



## Diplomarbeit

# Neutral Na beam plasma edge diagnostic at ASDEX Upgrade

Ausgeführt am Institut für Allgemeine Physik  
der Technischen Universität Wien

**unter der Anleitung von:**

Univ.-Prof. Dr. Friedrich Aumayr  
Univ.-Doz. Dr. Elisabeth Wolfrum

durch  
Josef Kamleitner  
Schwadorf 3  
A-3100 St. Pölten

Mai 2009



## Abstract

In Tokamak and Stellarator experiments on magnetic confined fusion the behavior of the plasma edge is very important for the characteristics of the whole plasma and for plasma wall interaction. Therefore diagnostics on the plasma edge are indispensable, they have to offer data at a high quality level to enable reasonable analysis of the plasma. The necessary high temporal and spatial resolution can only be reached by active diagnostics, like spectroscopy using neutral atoms beams.

The Li beam impact excitation spectroscopy (Li-IXS) delivers routinely electron density profiles and the Li beam charge exchange spectroscopy (Li-CXS) provides ion temperature and density profiles for selected discharges. Several advantages of replacing Li with Na are expected for these diagnostics. After a complete dataset of plasma particles - Na collisions is available [1], first experiments with combined Li/Na beams are carried out. So without disturbing the Li-IXS the validity of the underlying database is proven and a first view on the capabilities of the Na beam is given. Optical filters are purchased and the diagnostics program codes are adapted for Na beams. The influences of electron temperature and plasma impurity profiles are analyzed and considered to be low, while dedicated Na-IXS experiments are run for several weeks of operation.

The acquired data on a wide range of plasma discharges at ASDEX Upgrade, including the Standard and Improved H-Mode as well as He and H plasmas, enable a detailed analysis of the Na-IXS capabilities. In the main application, electron density evaluation on the plasma edge of deuterium H-Mode discharges, the Li beam performance is nearly equaled, but not exceeded by the Na beam, mainly due to the slightly deteriorated beam penetration depth. However, in other fields, like He plasma edge electron density, the Na beam could surprisingly top the Li beam capabilities.

## Kurzfassung

In Tokamak und Stellarator Experimenten an magnetisch eingeschlossenen Kernfusionsplasmen ist das Verhalten der Plasmarandschicht sehr wichtig für die Eigenschaften des gesamten Plasmas und der Plasma-Wand-Wechselwirkung. Daher sind Diagnostiken, die Daten hoher Qualität über die Plasmarandschicht liefern, unverzichtbar für eine sinnvolle Analyse des Plasmas. Die notwendige hohe zeitliche und räumliche Auflösung kann nur von aktiven Diagnostiken erreicht werden, wie die Spektroskopie von neutralen Atomstrahlen.

Die Lithiumstrahl Stoßanregungsspektroskopie (Li-IXS) liefert routinemäßig Elektrondichteprofile und die Lithiumstrahl Ladungsaustausch-spektroskopie (Li-CXS) stellt für ausgewählte Entladungen Ionendichte- und -temperaturprofile zur Verfügung. Durch den Ersatz von Lithium durch Natrium erwartet man sich einige Vorteile für diese Diagnostik. Nach der Verfügbarkeit eines kompletten Datensatzes von Plasmateilchen-Natrium-Stößen [1] werden erste Experimente mit gemischten Li- / Na- Strahlen durchgeführt. So wird die Validität der zugrundeliegenden Datenbasis bewiesen, ohne die Li-IXS zu stören, und ein erster Einblick in die Eigenschaften des Natriumstrahls gegeben. Optische Filter werden angeschafft und die Programmcodes der Diagnostik werden für Na Strahlen adaptiert. Der Einfluss der Elektronentemperatur und -dichte wird analysiert und für niedrig befunden, während dezidierte Na-IXS Experimente für die Dauer einiger Wochen durchgeführt werden.

Die erworbenen Daten auf einem weiten Bereich der Plasmaentladungen an ASDEX Upgrade, welche Standard und Improved H-Moden genauso wie He und H Plasmen enthalten, ermöglichen eine detaillierte Analyse der Eigenschaften und Möglichkeiten der Na-IXS. In der Hauptanwendung, Elektronendichteauswertung am Plasmarand von Deuterium H-Mode Entladungen, wird die Lithiumstrahl-Performance vom Natriumstrahl beinahe erreicht, aber nicht übertroffen, vor allem wegen der geringfügig reduzierten Eindringtiefe des Strahls. Jedoch konnte der Natriumstrahl in anderen Bereichen, wie etwa Elektronendichtemessung der Randschicht von He Plasma, überraschenderweise die Fähigkeiten des Lithiumstrahls überbieten.

# Contents

<b>1</b>	<b>Introduction</b>	<b>7</b>
1.1	Nuclear Fusion . . . . .	7
1.2	ASDEX Upgrade . . . . .	8
1.3	Plasma edge diagnostics . . . . .	9
1.4	Structure of this diploma thesis . . . . .	10
<b>2</b>	<b>Experimental setup</b>	<b>13</b>
2.1	General setup of Li/Na beam diagnostic at ASDEX Upgrade . .	13
2.1.1	Doppler shift for lower and upper optics . . . . .	16
2.1.2	Temporal resolution and chopping period . . . . .	16
2.2	Specification of Na beam diagnostic and expected advantages compared to Li . . . . .	17
2.2.1	Different refraction . . . . .	18
2.2.2	Na beam filter specifications . . . . .	20
<b>3</b>	<b>Collisional rates</b>	<b>21</b>
3.1	Rate coefficients for collisions of Na atoms with electrons and protons . . . . .	21
3.1.1	Implementation of the rate coefficient calculation . . . . .	24
3.2	Rate coefficients for collisions of Na with impurity ions . . . . .	24
<b>4</b>	<b>Modeling</b>	<b>29</b>
4.1	Implementation of the beam attenuation modeling . . . . .	30
4.2	Examples . . . . .	31
<b>5</b>	<b>Calculation of electron density</b>	<b>35</b>
5.1	Program absolut / shooting method . . . . .	35
5.1.1	Rearrangement of the modeling equation . . . . .	35
5.1.2	The singularity condition / point of singularity . . . . .	36
5.1.3	Implementation of the program absolut . . . . .	37
5.2	Diagnostic LID / shooting method . . . . .	37
5.3	Diagnostic LIN / Bayesian Ansatz . . . . .	38
5.4	Diagnostic IDA / integrated data analysis with Bayesian Ansatz	40
<b>6</b>	<b>Dependence on secondary input data</b>	<b>41</b>
6.1	Dependence on electron temperature ( $T_e$ ) profiles . . . . .	41
6.2	Dependence on $Z_{eff}$ profiles . . . . .	42

<b>7</b>	<b>Experimental results</b>	<b>47</b>
7.1	First campaign (Na:Li=1:9)	47
7.2	Second campaign (Na:Li=9:1)	48
7.2.1	Standard H-Mode discharges	49
7.2.2	Na beam compared to Edge Thomson Scattering and Li beam diagnostics in Improved H-Mode discharges	53
7.2.3	L-Mode discharges	53
7.3	Third campaign (pure Na)	58
7.3.1	Standard H-Mode discharges	58
7.3.2	Higher beam energies	60
7.3.3	He campaign	60
7.3.4	H campaign	63
<b>8</b>	<b>Conclusions</b>	<b>65</b>
8.1	Results on expected advantages and disadvantages in Na beam operation	65
8.1.1	Emitter temperature	65
8.1.2	Neutralization efficiency	65
8.1.3	Charge exchange cross sections	66
8.1.4	Shorter transition lifetime	66
8.1.5	Effects of the different wavelength	66
8.1.6	Atomic mass	67
8.1.7	Lower ionization energy	67
8.2	Summarizing the comparison to Li beam	67
8.2.1	Penetration and $n_e$ evaluation depth	67
8.2.2	$n_e$ evaluation quality	67
8.2.3	Non-standard plasmas	68
8.2.4	Influence on the plasma	68
8.2.5	Future plans	68
<b>A</b>	<b>General appendix</b>	<b>69</b>
A.1	Sellmeier series equation	69
A.1.1	beam coordinates	69
<b>B</b>	<b>Implementation of the main programs</b>	<b>71</b>
B.1	Implementation of the rate coefficient calculations	71
B.2	Implementation of the beam attenuation modeling	72
B.3	Implementation of the program absolut	74
B.4	Changes in the implementation of the new probabilistic evaluation algorithm	77
<b>C</b>	<b>Programs used for data processing, evaluation and visualization</b>	<b>79</b>
C.1	IDL programs	79
C.2	MATLAB functions	79
C.2.1	data reading functions	80
C.2.2	data processing functions	80
C.2.3	plotting functions	80

# Chapter 1

## Introduction

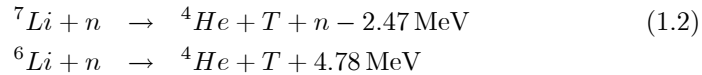
### 1.1 Nuclear Fusion

Nuclear fusion is the energy source of stars like the sun, and nowadays a very large fraction of energy consumed on earth has its origin in the radiation arriving from the sun. Nuclear fusion is the fusion of two light nuclei to one heavier nucleus. In most of these processes for light nuclei, binding energy and additional particles (like neutrons or protons, carrying the main part of the energy) are released. Since the time these processes have been discovered and understood there are plans to use them as a source of energy in commercial power plants. While the first fission power plants have already produced energy for several decades, it turned out, that a nuclear fusion power plant is much more challenging. The most promising approach is thermonuclear fusion, where plasmas are confined at high temperatures.

The fusion reaction with the cross section leading to the highest fusion rates under terrestrial achievable conditions is the following [2]:



While deuterium  $D$  (a heavier isotope of hydrogen  $H$ ) is available in sea water in huge amounts the short-living tritium  $T$  has to be bred from lithium  $Li$  using the following reactions [2]:



To use nuclear fusion as an energy source it is necessary to get more energy out of the fusion reactions than is needed to sustain the reaction conditions and is lost during conversion of binding energy in heat and finally electrical energy. Ignition of the plasma is reached, if the fusion reaction is sustaining itself. The main condition that has to be fulfilled to reach energy amplification or even ignition is to keep the so-called "triple product" of ion density  $n_i$ , ion temperature  $T_i$  and energy confinement time  $\tau_E$  high enough (Lawson criterion) [3]:

$$n_i \cdot T_i \cdot \tau_E > 10^{22} \frac{\text{keV s}}{\text{m}^3} \quad (1.3)$$

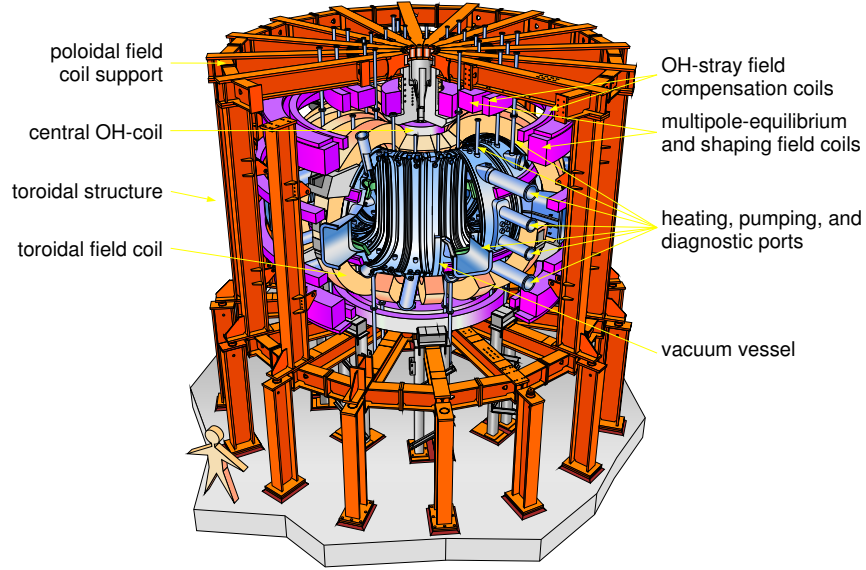


Figure 1.1: ASDEX Upgrade, description of the main (structural) components and coils [4].

One way of confining the plasma is the magnetic confinement, done in toroidal configurations. Here the two main concepts are the Tokamak (like ASDEX Upgrade, fig. 1.1) and the Stellarator (like W7-X, fig. 1.2). In both machines the confinement is achieved by a toroidal and a poloidal magnetic field. While the poloidal component is produced by additional external coils or very specially shaped coils in a Stellarator, the Tokamak uses an induced plasma current for the poloidal field component. The plasma current in a Tokamak is also an efficient way of heating up the plasma (ohmic heating), but it can only be kept for a limited pulse period because it is induced by the central OH-coil. Depending on the Tokamak the pulse lengths lie within several seconds and one hour. [2], [3], [4]

## 1.2 ASDEX Upgrade

ASDEX Upgrade (*Axialsymmetric Divertor Experiment*, also abbreviated as AUG, fig. 1.1) is a medium sized Tokamak (major radius  $R = 1.65\text{ m}$ , minor radius  $a = 0.5\text{ m}$ ) at the Max Planck Institute of Plasma Physics in Garching / Germany with high external heating power (up to 28 MW) and a pulse length of up to 10 seconds, in operation since 1991. It is an ITER-like configuration, with high shaping capability and single or double null divertor. In 1996 a tungsten coated divertor was installed and since 2008 ASDEX Upgrade is a full tungsten machine (first wall). Its predecessor ASDEX was the first machine operating in the high confinement mode (H-Mode). ASDEX Upgrade still enhances performance with advanced plasma scenarios like the "improved H-Mode" and non-inductive current drive. Another important field is the control



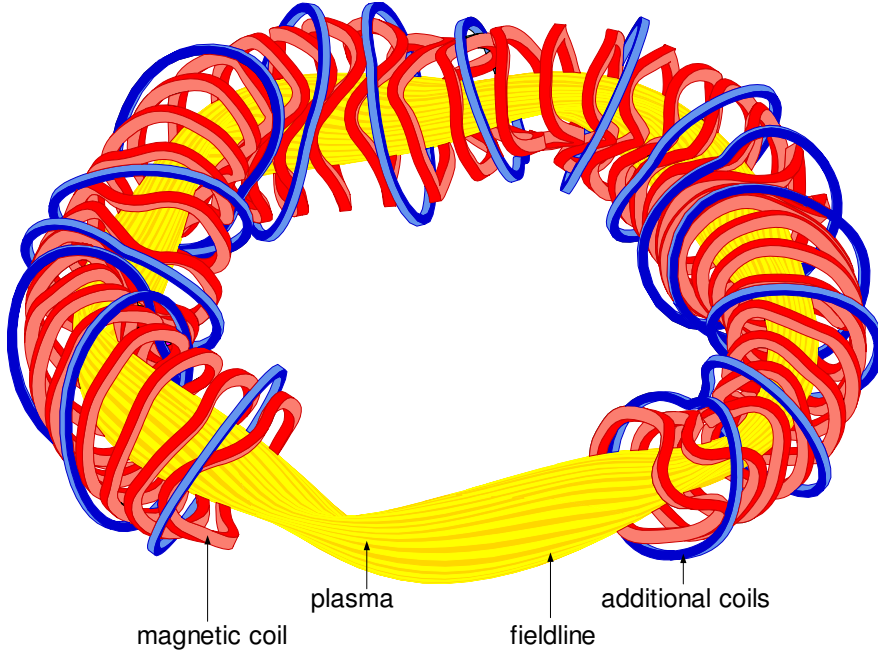


Figure 1.2: design of the superconducting Stellarator W-7X showing field lines and magnetic coils [4].

and mitigation of edge localized modes (ELMs). [4], [5]

### 1.3 Plasma edge diagnostics

The so-called plasma edge is the outer region of the plasma. It is the area around the separatrix, the border between the closed flux surfaces inside the plasma and the open flux lines that end up in the divertor. This latter region is called Scrape Off Layer (SOL).

The investigation of the plasma edge is very important in each fusion device. For H-Mode investigations (for instance at ASDEX Upgrade), the steep gradients of electron density  $n_e$  and electron temperature  $T_e$ , occurring in the edge transport barrier (ETB) zone, are of special interest. These gradients have to be analyzed by diagnostics of high spatial resolution ( $< 10$  mm). A high temporal resolution is necessary for a detailed investigation of ELMs ( $< 1$  ms).

For most plasma parameters, as for instance electron density, these requirements can only be met by "active" diagnostics. Diagnostics for electron density measurements use for example Thomson scattering of Laser beams [6], [7], reflection of microwaves [8], [9] or runtime-delay of infrared light. Another possibility is to measure the interaction of neutral atom beams with the plasma [10], [11], [12]. Concerning the plasma core neutral H-beams used for plasma heating are also used for diagnostic purposes. In the plasma edge Li or Na beams are used [13], [14], [15], [16]. The interaction leads to characteristic line emission, its spatial intensity profile contains the information about the plasma.

Combining different diagnostics that measure the same plasma parameter is used to increase the performance (quality, accuracy, resolution or range) (see 5.4, [17]).

### Coordinate systems

In ASDEX Upgrade a set of different coordinate systems is used, each is ideal for a certain application or diagnostic. In the following the coordinates used in this work will be listed, defined and described:

$(R_{maj}, \tilde{z})$  The major radius  $R_{maj}$  and the height from the magnetic midplane  $\tilde{z}$  form the main cylindrical coordinate system in ASDEX Upgrade, the usual unit is m. Because of the axial symmetry in most applications the toroidal angle as third coordinate is neglected.

$\rho_{pol}$  The normalized poloidal radius  $\rho_{pol}$  is zero at the central plasma flux line and 1 at the separatrix position. It describes the relative position in the plasma in one dimension, the related poloidal angle plays a minor role. Because the plasma position and shape varies within discharges the transformation to the  $(R_{maj}, z)$ -system also changes. These transformations are provided by plasma diagnostics with temporal resolutions of several ms.

$R_{midplane}$  measures the radial position, mapped to the magnetic midplane ( $z = 0$ ), in terms of  $R_{maj}$ .

$z$  in the context of the Na/Li-beam diagnostic is the beam coordinate, varying from 0 to 15 cm. Sometimes it is also called  $x$ . The origin lies close the outermost observed beam position, the innermost channel is near 15 cm. The beam coordinate is used internally in the Na/Li-beam evaluation and modeling programs and can be easily transformed to the  $(R_{maj}, z)$  system and further to other coordinates.

## 1.4 Structure of this diploma thesis

**Chapter 1** gave an introduction on the topic

**Chapter 2** describes the experimental setup of the Li/Na beam diagnostic at ASDEX Upgrade. The expected advantages of the use of Na as compared to Li are pointed out.

**Chapter 3** is about the rate coefficients for collisions of Na atoms with plasma particles and their calculation.

**Chapter 4** explains the Na beam attenuation modeling and gives first examples.

**Chapter 5** describes the different algorithms applied for electron density calculation, namely the shooting method and the Bayesian Ansatz.

**Chapter 6** deals with the dependence of electron density evaluation on secondary input data like plasma temperature and impurities.

**Chapter 7** lists and discusses the experimental results acquired within 3 Na beam campaigns at ASDEX Upgrade.

**Chapter 8** points out if the several expectations towards the Na beam could be fulfilled and gives a summarized comparison between Na and Li beam.

**Appendix** In the appendix the beam coordinate change due to different refraction is quantified and all relevant implementation details of the used evaluation programs are listed.

Some result of this thesis have already been published: [18]



## Chapter 2

# Experimental setup

### 2.1 General setup of Li/Na beam diagnostic at ASDEX Upgrade

The Lithium beam diagnostic at ASDEX Upgrade delivers routinely edge electron density ( $n_e$ ) profiles and ion temperature ( $T_i$ ) and density ( $n_i$ ) profiles for selected shots. The setup consists of three main parts: The beam line producing the neutral beam, the two optical heads with attached optical instruments and the programs calculating the requested data from the measured data.

The beam production works as follows: Li-Ions are emitted from a heated  $\beta$ -eucryptite ( $LiAlSiO_4$ ) cathode and accelerated in two steps up to energies of usually 40 – 60keV. The focused beam passes through a beam chopper (deflection plates) that allows to pulse the beam to allow background radiation measurements. Then the Li-Ions beam is neutralized in a sodium cell. This is necessary because otherwise the strong magnetic field in ASDEX Upgrade would deflect the beam when it leaves the iron-shielded beam production part. The neutralized Li beam then passes through a shutter into the main vessel of ASDEX Upgrade and collides with plasma particles. The position and direction of the beam is shown in figures 2.1, 2.2.

Photons emitted in the course of these collisions are observed by two optical heads, one on the upper part of the vessel, the other on the lower part, as shown in figure 2.1. From both optical heads the light is guided outside through optical fibres. The upper optics consist of 35 fibre channels equipped at the end with filters and photomultipliers and is called IXS (impact excitation spectroscopy). It is routinely used to provide electron density profiles at high spatial (5 mm) and temporal (50  $\mu$ s) resolution. The lower optics consist of 18 fibre channels that are split and guided to 2 Czerny-Turner-spectrometers connected to frame transfer(EM-)CCD cameras. The lower optics is called CXS (charge exchange spectroscopy) and mainly used for measuring impurity ions [19], [20], [21], [22], [23]. It can also be used for deriving electron density profiles, but with lower spatial and temporal resolution than the IXS. 4 channels of the lower optics are used for density fluctuation measurements. Passive applications like measuring the radial electric field by the Doppler-shift of a He-line are also possible [24].

The measured data of the IXS are written into the shotfile as diagnostic LIB, the raw data of the lower optics are written to LIA and LIC. Out of these

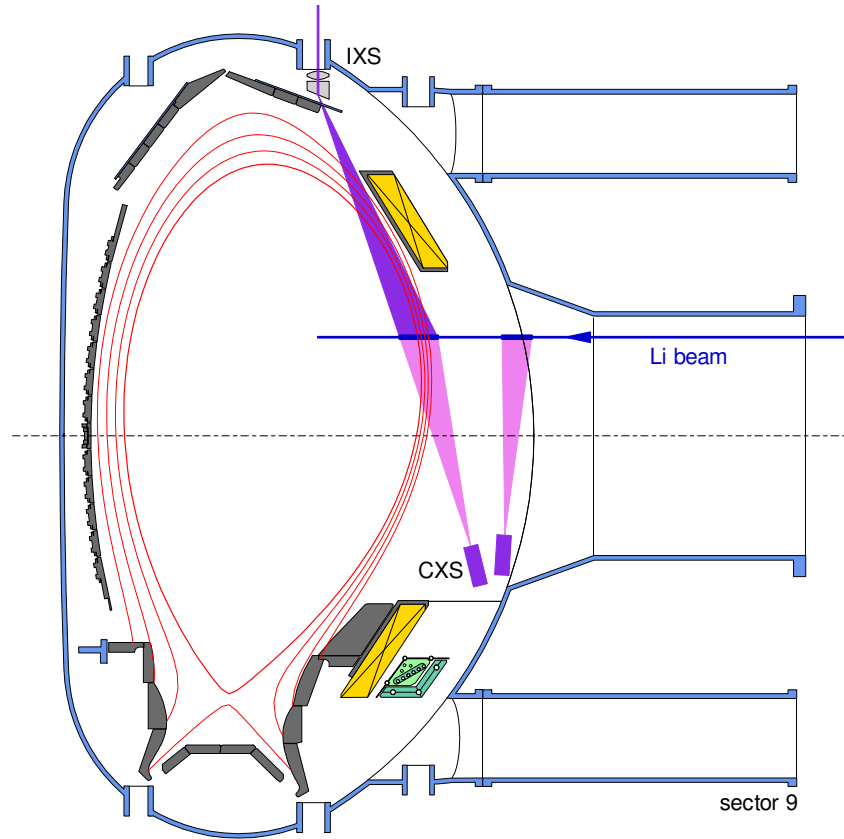


Figure 2.1: poloidal cut through the vacuum vessel of ASDEX Upgrade in the plane of the Li beam diagnostic [4].

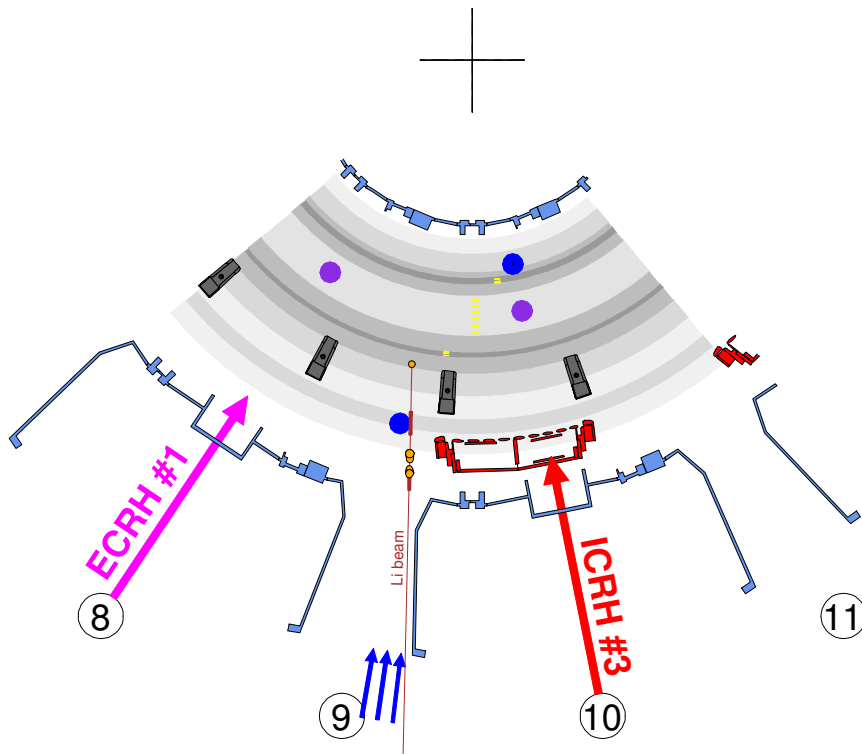


Figure 2.2: toroidal view (from above) at the quarter section of ASDEX Upgrade, where the Li beam diagnostic is positioned [4].

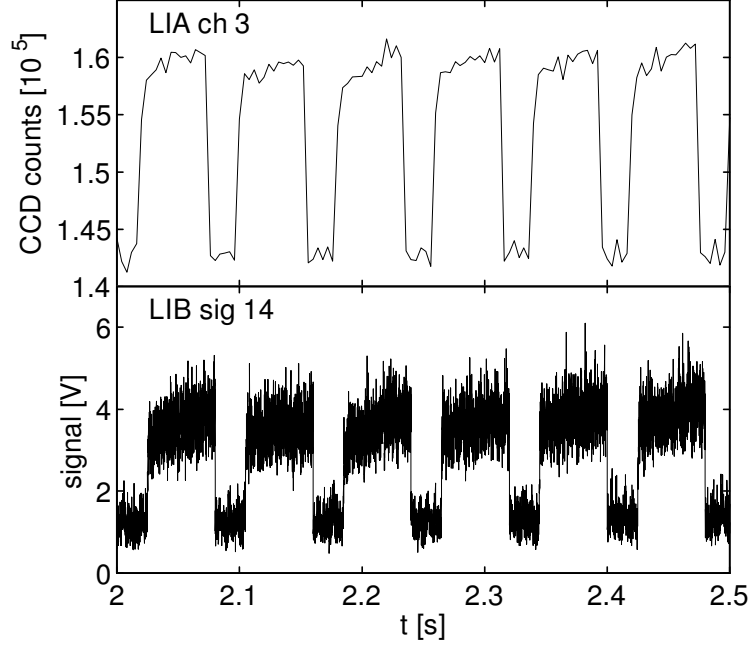


Figure 2.3: Typical time traces (AUG # 23074) for the lower optics (LIA, units: CCD counts) and the upper optics (LIB, signal voltage) showing time intervals where the beam is "on" and "off".

data a number of different algorithms can provide the requested profiles. For electron density calculations the methods named diagnostics LID, LIN and IDA (see chapter 5) are used routinely. For this work a similar program was adapted to provide electron density profiles from LIA and LIC data (see also [25]).

### 2.1.1 Doppler shift for lower and upper optics

Due to the motion of the beam atoms relative to the direction of observation, the emitted light is Doppler shifted. Both optics have in principle different lines of sight: The lower optic observes the beam from the back, while the upper optic observes the beam from the front (see fig. 2.1, 2.4). Additionally the observing angle differ slightly from channel to channel. For the upper optics and the Na beam the shift is between  $-0.42$  nm (Li:  $-0.67$  nm) for channel 35 and  $-0.63$  nm (Li:  $-1.01$  nm) for channel 1. For the lower optics the shift is positive with similar absolute values.

### 2.1.2 Temporal resolution and chopping period

As already mentioned in 2.1, a beam chopper is used to stop the beam for 24 ms within a period of 80 ms, resulting in "beam on" periods of 56 ms. The temporal resolution of the lower optics with 4 ms is smaller than for the upper optics with



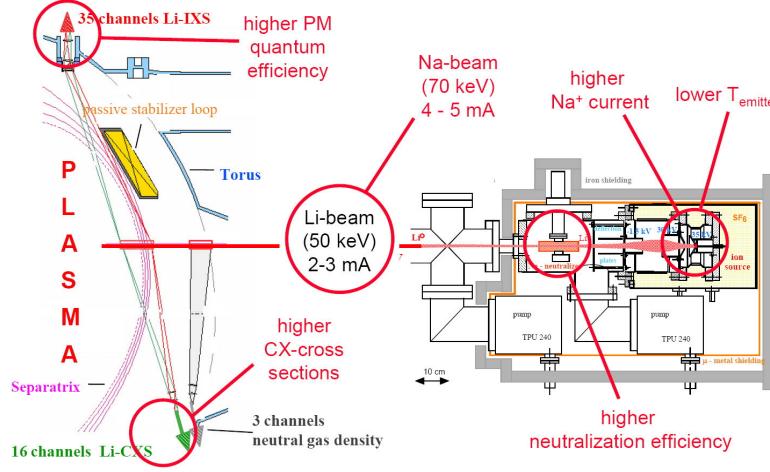


Figure 2.4: The experimental setup of the Na/Li beam diagnostic at ASDEX Upgrade

a scanning frequency of 20 kHz, corresponding to a resolution of  $50 \mu\text{s}$ . Typical time traces for the two diagnostics are shown in figure 2.3. In future the chopper will be improved, to be able to provide shorter on/off periods.

## 2.2 Specification of Na beam diagnostic and expected advantages compared to Li

The main setup (fig. 2.4) as described in the previous section for the Li beam stays the same for the Na beam. The  $\beta$ -eucryptite powder for the cathode is fully or partially replaced by  $\text{NaAlSiO}_4$  and the voltage at the deflection plates has to be adjusted. At the upper optics the filters for the Li I (2p-2s) line are replaced by filters for the Na I (3p-3s) line. At the lower optics the spectrometers only have to be moved to the respective Na-wavelength. A certain amount of changes is also necessary in the programs evaluating the measured data because of the different atomic data of Na and Li.

These differences in atomic data lead to the main advantages (and disadvantages) that have to be expected when replacing Li with Na (see also Fig. 2.4):

1. Due to differences in vapor pressure for Na the emitter temperature can be kept lower than for Li. So the withstand voltage rises and the stability of the ion source at higher voltages ( $\geq 60 \text{ keV}$ ) is improved. A higher current may be achieved at higher extraction voltages or by raising the temperature to the Li level.
2. The neutralization of the ion beam occurs for both Li and Na in a Na cell. Because the charge exchange cross section between  $\text{Na}^+$  and  $\text{Na}^0$  is resonant and therefore higher than between  $\text{Li}^+$  and  $\text{Na}^0$ , a higher

neutralization efficiency is achieved. This allows to drive the beam with a higher current and to reduce the Na density in the charge exchange cell.

3. The charge exchange cross sections for collisions with relevant impurity ions like He and C are usually larger, facilitating ion temperature measurements more easily.
4. The lifetime of the transition observed for electron density measurements is shorter for Na than for Li (Na I (3p-3s): 16.2 ns, Li I(2p-2s): 26.9 ns). This is of benefit for the planned density fluctuation measurement. The shorter lifetime does not raise the emission intensity significantly, because the excited Na state is less occupied than the Li one. But this resulting lower occupation of excited states reduces the Na beam attenuation, because the very effective charge exchange and ionization from these states plays a minor role.
5. The wavelength of the Na I (3p-3s) transition (@588.9 nm in the yellow region) differs from the Li I (2p-2s) transition (@670.8 nm). This leads to several effects:
  - (a) The used photomultipliers are more sensitive in the yellow region improving the signal-to-noise ratio in the case of Na.
  - (b) The background radiation (mainly from impurity ions like He) in the wavelength regions of the transitions are different. This has to be taken care of in the filter specifications, leading to a slightly higher maximal transmission in the case of Li, because the Na filters have to cut out the He I line @587.6 nm.
  - (c) It still has to be checked if the radiation from thermal Na, that diffuses from the neutralization cell into the vessel, leads to negative effects (increased background).
  - (d) The refraction is different for the Li and the Na line, so that the IXS-observed beam coordinates differ by about 2 mm.
6. The atomic mass of Na is with 22.99 u higher than of Li with 6.94 u. So for same beam energies the beam velocity is lower, raising the question, if the Na beam will penetrate as deep as the Li beam. On the other hand lifetime smearing is also reduced, being beneficial for fluctuation measurements.
7. The ionization energy for Na is slightly lower than for Li. This may also influence the penetration depth.

In chapter 8 it is discussed whether these expectations are actually fulfilled or not. Some facts are now described in more detail:

### 2.2.1 Different refraction

In the upper optics the light has to pass a prism and two lenses before reaching the optical fibres (see fig. 2.5). So the observed beam coordinate of each fibre depends on refraction in these optical instruments. The refraction index itself depends on the observed wavelength and differs between 1,5055 for Li (2p-2s) emitted light and 1,5084 for Na (3p-3s) emitted light.

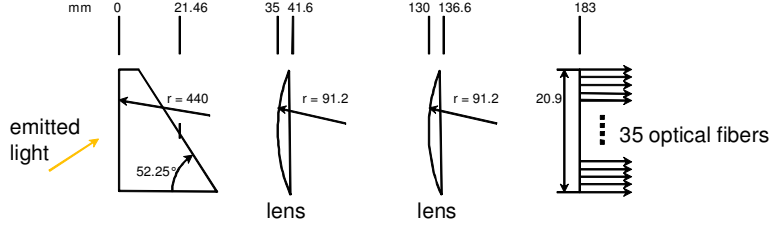


Figure 2.5: The geometry of the upper optics

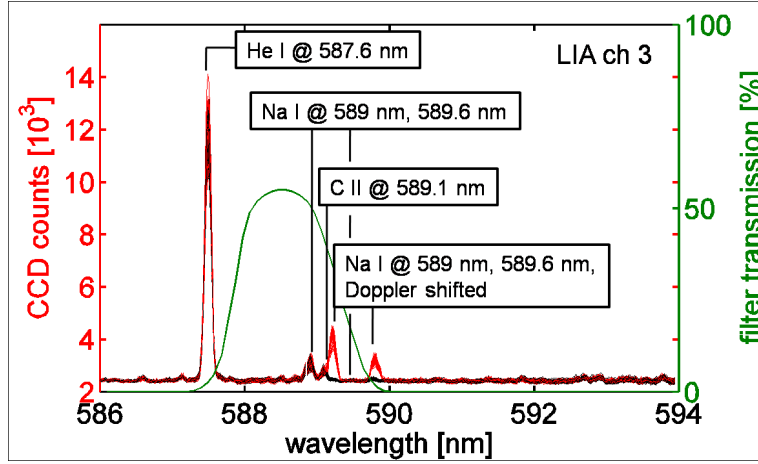


Figure 2.6: Left axes: Typical spectra (AUG 23074, LIA ch 3) at beam on (red) and beam off (black) period taken with the lower optics. Right axes: Filter transmission curve (green) for the filters used in the upper optics filter-PM-system.

The beam coordinates of the observed points along the injected beam have been individually measured for the Li line. Out of these data and the exact geometry of the optical system the refraction index for the Li line is evaluated. This is necessary because the glass type has not been documented and the refraction index has already changed over the years of operation due to irradiation (neutrons, ...). The refraction behavior best fits to the Schott glass N-ZK7 [26]. The Sellmeier series equation (see A.1) with coefficients for this glass type was used then to calculate the refraction index for the Na line.

So the observed beam coordinates for the Na line can be easily derived and differ about 2 mm as compared to the observed beam coordinates for the Li line. The detailed coordinate table (table A.1) is shown in A.1.1.

### 2.2.2 Na beam filter specifications

Figure 2.6 shows typical spectra as observed by the lower optics for beam on and beam off periods. The following filter specifications are required for the upper optics: The transmission at the He I line @ 587.6 nm should be lower than 5%, while the transmission should be best for the Na I doublet line @ 589 nm and 589.6 nm, Doppler-shifted by about half a nm to shorter wavelength. As can be seen in fig. 2.6, these requirements are fulfilled by the shown measured transmission curve of the filters purchased and used for Na beam diagnostics. The only problem is the remaining C II line @ 589.1 nm, occurring strongly in H campaigns where  $CH_4$  is used (see 7.3.4). For D discharges this problem does not arise since the C II line is very weak in ASDEX Upgrade as a full tungsten machine. For He campaigns it is a question, whether the transmission of 5% for the He I line is low enough to suppress it successfully. This question will be answered in 7.3.3.

## Chapter 3

# Collisional rates

For the Na beam attenuation modeling (chapter 4) all collisions of the neutral beam atoms with plasma particles have to be taken into account. This includes electron, proton and impurity ion impact excitation, ionization and charge exchange processes. Cross sections for these processes have been derived in [1] (some typical examples are shown in figures 3.1-3.4). Collisional rates are then calculated from these cross sections.

In the case of Na, 9 states are taken into account in the modeling: Na 3s, 3p, 4s, 3d, 4p, 5s, 4d, 4f and  $\text{Na}^+$ , enumerated as states  $i = 1$  to  $i = 9$ .

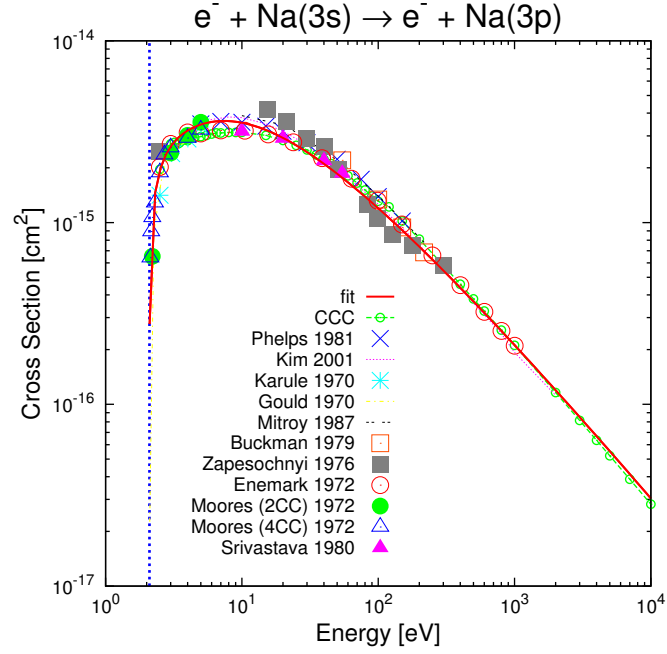
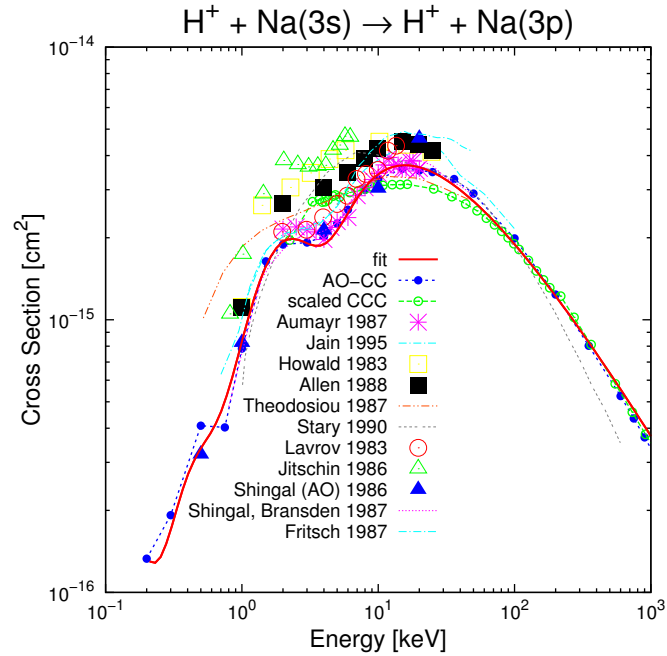
### 3.1 Rate coefficients for collisions of Na atoms with electrons and protons

Based on procedures used to calculate rate coefficients for the Li beam (see [27], [28], database in [29], [30]) the respective programs are adapted and improved for calculation of rate coefficients for the Na beam, using the cross section data from [1] as an input.

The rate coefficients  $R_{i \rightarrow j}^x = \langle \sigma v \rangle$ ;  $x = e^-, p^+$  describe the number of excitations ( $i < j$ ), de-excitations ( $i > j$ ) and ionizations / electron loss ( $j = N$ ) of a Na atom in state  $i$  due to collisions with  $e^-$  and  $p^+$  in units of volume per time.  $\sigma$  is the corresponding cross section for the process and dependent on the relative velocity of Na and the plasma particles  $v$  and the brackets  $\langle . \rangle$  mean averaging over the relative velocity distribution. The relative velocity  $v$  is the absolute value of the difference between the beam velocity  $v_{beam}$  defined by the beam energy  $E_{beam}$  and the velocity of the plasma particles  $\vec{v}_x$ , that is described by a velocity distribution  $f(\vec{v}_x)$ , depending on plasma temperature  $(T_e, T_i)$ .

$$\begin{aligned} R_{i \rightarrow j}^x &= \langle \sigma(v) v \rangle = \int_{\mathbb{R}^3} \sigma(v) v f(\vec{v}_x) d^3 v_x \\ v &= \|\vec{v}_{beam} - \vec{v}_x\|_2 \\ x &= e^-, p^+ \end{aligned} \quad (3.1)$$

It is supposed that  $T := T_i = T_e$  and that  $\vec{v}_x$  can be described by a Maxwell

Figure 3.1: Electron excitation cross sections for Na  $3s \rightarrow 3p$ , from [1]Figure 3.2: Proton excitation cross sections for Na  $3s \rightarrow 3p$ , from [1]

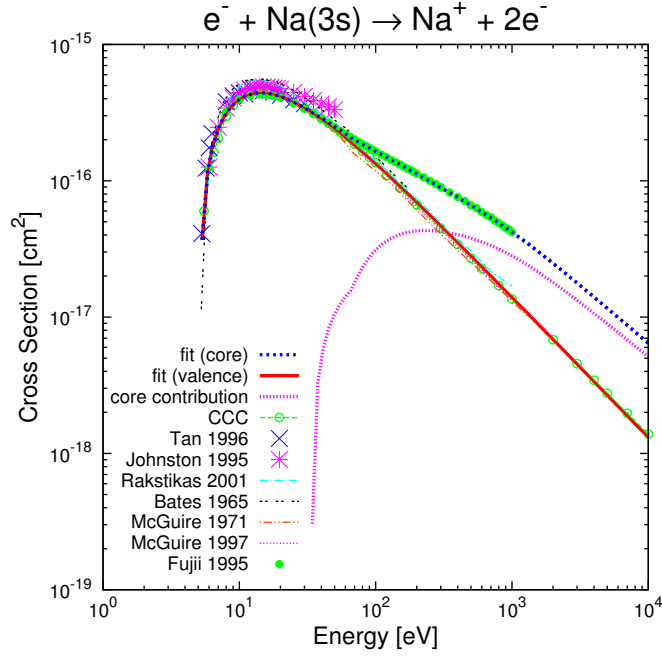


Figure 3.3: Electron-Impact Ionization from Na(3s), from [1]

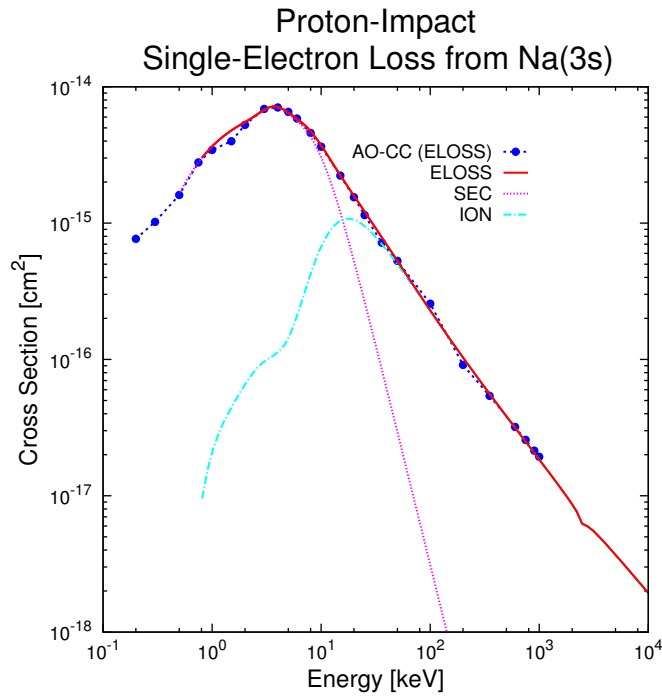


Figure 3.4: Proton-Impact Single-Electron Loss from Na(3s), from [1]

distribution.

$$f(\vec{v}_x) = f(v_x) = \frac{1}{(\sqrt{\pi}w_x)^3} \exp \left[ - \left( \frac{v_x}{w_x} \right)^2 \right] \quad (3.2)$$

$$w_x = \sqrt{\frac{2k_B T}{m_x}}$$

The formula for the rate coefficient ( $i < j$ ) then becomes:

$$R_{i \rightarrow j}^x = \int_0^\infty v^2 \sigma(v) \left\{ \exp \left[ - \left( \frac{v - v_{beam}}{w} \right)^2 \right] - \exp \left[ - \left( \frac{v + v_{beam}}{w} \right)^2 \right] \right\} dv \quad (3.3)$$

The rate coefficients for de-excitation can be easily derived from the rate coefficients for excitation using the formulas

$$R_{j \rightarrow i}^{e-} = R_{i \rightarrow j}^{e-} \frac{g_i}{g_j} \exp \left( \frac{\Delta E_{i \rightarrow j}}{k_B T_e} \right) \quad (3.4)$$

$$R_{j \rightarrow i}^{p+} = R_{i \rightarrow j}^{p+} \frac{g_i}{g_j} \quad (3.5)$$

again for  $i < j$ . As mentioned above, these rate coefficients  $R_{i \rightarrow j}^x$  ( $i \neq j$ ) describe rates in units of volume per time. To use them directly in the modeling differential equation (dependent on location, not time), they are divided by the beam velocity  $v_{beam}$ , giving the so-called reduced rates

$$r_{i \rightarrow j}^x = \frac{dt}{dz} R_{i \rightarrow j}^x = \left( \frac{dz}{dt} \right)^{-1} R_{i \rightarrow j}^x = \frac{R_{i \rightarrow j}^x}{v_{beam}} \quad (3.6)$$

in units of area (volume per length). Figure 3.5 and 3.6 show the rate coefficients and reduced rate coefficients for the processes / cross sections shown in figures 3.1, 3.2 for beam energies of 40, 60, 80 and 100 keV.

### 3.1.1 Implementation of the rate coefficient calculation

The calculation of the rate coefficients for collisions of Na with electrons and protons was implemented in two FORTRAN77-Subroutines, `elratna1-2.f` and `proratna1-2.f`. A description of the implementation is given in B.1.

## 3.2 Rate coefficients for collisions of Na with impurity ions

In fusion plasmas the impurity ion density is regularly described by two parameters,  $Z_{eff}$  and  $q$ . In general these parameters vary for different location (measured in beam coordinate  $z$  or normalized poloidal radius  $\rho_{pol}$ ).

$q$  is the mean charge of the impurity ions, and the effective charge  $Z_{eff}$  is defined [2] as

$$Z_{eff} := \frac{n_p + n_i q^2}{n_e} \quad (3.7)$$



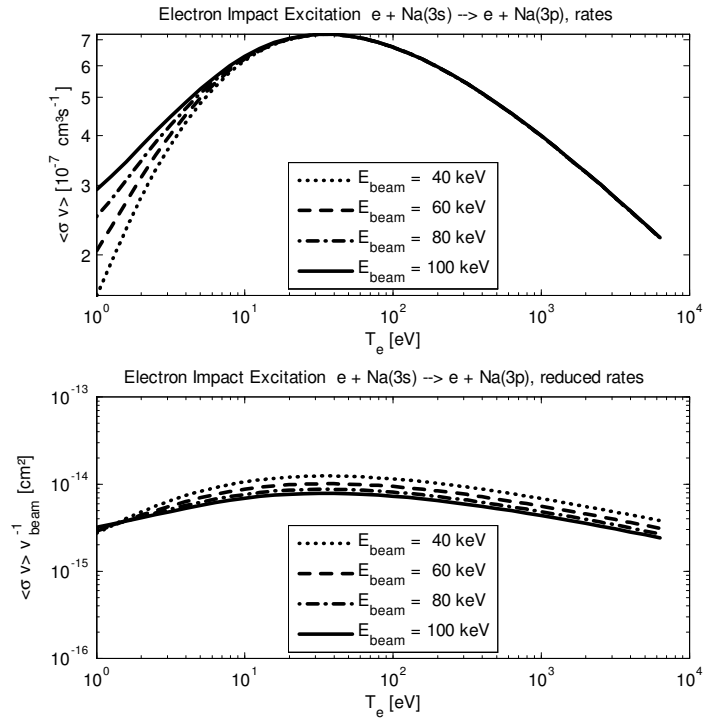


Figure 3.5: Electron excitation rates and reduced rates for  $\text{Na } 3s \rightarrow 3p$  and different Na beam energies  $E_{\text{beam}}$ .

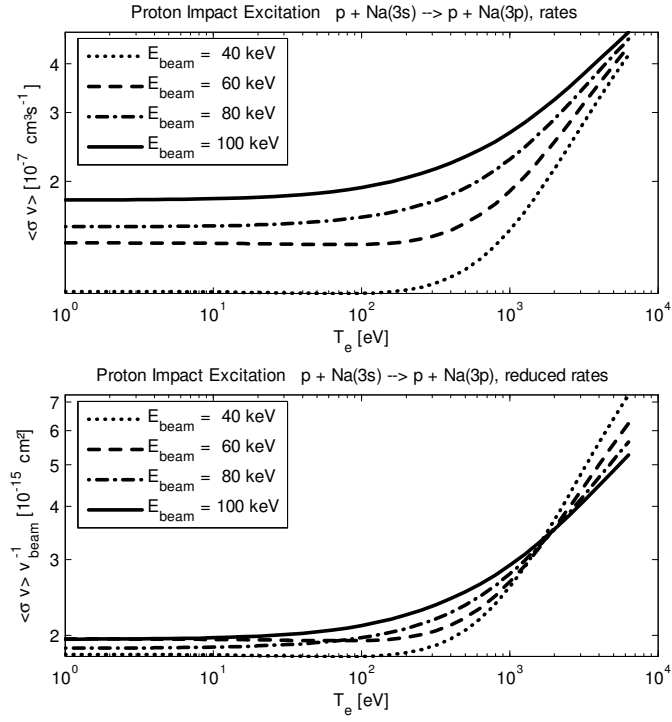


Figure 3.6: Proton excitation rates and reduced rates for  $\text{Na } 3s \rightarrow 3p$  and different Na beam energies  $E_{\text{beam}}$ .

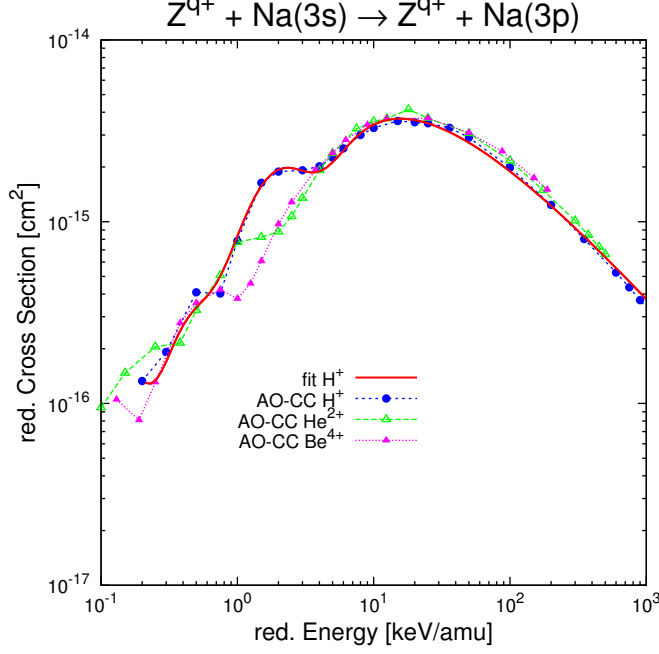


Figure 3.7: Ion-impact reduced excitation cross sections for Na  $3s \rightarrow 3p$ , from [1]

with proton density  $n_p$ , impurity ion density  $n_i$  and electron density  $n_e$ . If different types of impurity ions occur, the ion term in (3.7) turns into a sum over all ion types  $i$

$$Z_{eff} := \frac{n_p + \sum_i n_i q_i^2}{n_e} \quad (3.8)$$

For given  $n_e$ ,  $Z_{eff}$  and  $q$ ,  $n_i$  and  $n_p$  can be calculated using the fraction  $frac$ :

$$frac := \frac{Z_{eff} - 1}{q(q - 1)} \quad (3.9)$$

$$\begin{aligned} n_i &= frac \cdot n_e \\ n_p &= (1 - frac \cdot q) \cdot n_e \end{aligned} \quad (3.10)$$

The higher mass of impurity ions as compared to electrons or protons lead to a lower velocity. In this case the energy of collisions between impurity ions and Na can be approximated by the Na beam energy  $E_{beam}$ . So the reduced rates  $r_{i \rightarrow j}^x = \frac{\langle \sigma(v)v \rangle}{v_{beam}}$  for  $x = i$  (ion) are replaced by the cross sections  $\sigma(v_{beam}) = \sigma(E_{beam})$ , no further calculations are necessary:

$$r_{i \rightarrow j}^i = \sigma(E_{beam}) = \sigma_{i \rightarrow j}(E_{beam}, q) \quad (3.11)$$

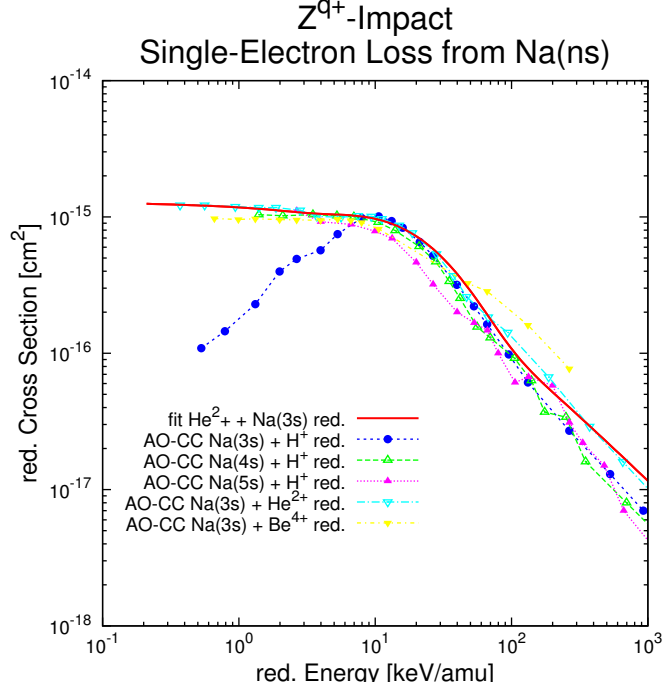


Figure 3.8: Ion-Impact reduced Single-Electron Loss cross sections for Na(3s), from [1]

The cross sections for collisions of impurity ions with Na can be easily derived from cross sections for Na atoms colliding with protons and  $He^+$  using scaling relations [1]. These relations are:

$$\begin{aligned} E_{red.}^{EXC} &= \frac{E}{n^2} & \sigma_{red.}^{EXC} &= \frac{\sigma}{n^4} \\ E_{red.}^{ELOSS} &= \frac{n^2 E}{\sqrt{q}} & \sigma_{red.}^{ELOSS} &= \frac{\sigma}{n^4 q} \end{aligned} \quad (3.12)$$

with  $n = \frac{1}{\sqrt{2E_b}}$  and the binding energy  $E_b$ .  $m_{beam}$  is the mass of a Na atom in atomic mass units u. The reduced cross sections are shown in figures 3.7 and 3.8.

Substitution of the relations (3.12) into (3.11) leads to the rate coefficients for Na excitation and electron loss due to collisions with impurity ions:

$$\begin{aligned} r_{i \rightarrow j}^i &= q \cdot \sigma_{red.}^{EXC} \left( \frac{E_{beam}/m_{beam}}{q} \right), \forall i, j < N \\ r_{i \rightarrow j}^i &= n^4 q \cdot \sigma_{red.}^{ELOSS} \left( \frac{n^2 \cdot E_{beam}/m_{beam}}{\sqrt{q}} \right), \forall i < N, j = N \end{aligned} \quad (3.13)$$

Because of the low numerical effort compared to the calculation of the reduced rates for electrons and protons and due to the possible variation of  $Z_{eff}$  and  $q$ , the reduced rates for collisions of Na with impurity ions are directly implemented in the modeling (zmod\_nav1-0.f) and described in chapter 4.

## Chapter 4

# Modeling

The beam attenuation modeling describes the occupation numbers of important (excited) Na states and ionized Na atoms for a given  $n_e$ -profile. Further the electron temperature and impurity ion density profiles are necessary for the modeling (see chapter 6). The spatial occupation number densities  $N_i(z)$  are described by a system of linear differential equations:

$$\frac{dN_i}{dz} = \sum_{j=1}^N \{n_e(z) a_{ij}(T_e(z)) + b_{ij}\} N_j(z) \quad (4.1)$$

$$N_i(z=0) = \delta_{1i} \quad (4.2)$$

$N$  is the number of states taken into account (9 states: Na 3s, 3p, 4s, 3d, 4p, 5s, 4d, 4f,  $\text{Na}^+$ ) and  $i = 1, \dots, 9$  is the respective index of each state. The matrix  $a_{ij}$  contains the reduced rates for excitation, de-excitation and ionization due to collisions of Na with plasma particles (electrons, protons, impurity ions). The matrix  $b_{ij}$  consists of the reduced Einstein coefficients for spontaneous emission. The boundary condition describes that at  $z = 0$  all beam atoms are in the ground state Na 3s ( $i = 1$ ).

In detail, the coefficients  $a_{ij}$  are defined as follows:

$$a_{ij} = a_{ij}^e + (1 - \text{frac} \cdot q) a_{ij}^p + \text{frac} \cdot a_{ij}^i \quad (4.3)$$

$$\begin{aligned} a_{ij}^x &: = r_{j \rightarrow i}^x \geq 0, i < j < N \\ a_{ii}^x &: = - \left( \sum_{i > j} r_{i \rightarrow j}^x + \sum_{i < j} r_{i \rightarrow j}^x \right) \leq 0 \\ a_{ji}^x &: = r_{i \rightarrow j}^x \geq 0, i < j < N \end{aligned} \quad (4.4)$$

and describe changes of occupation numbers due to collisions. The definitions in (4.3) and (4.4) lead to the following form of the A-Matrix, consisting of an upper part  $U$ , the diagonal  $d$  and a lower part  $L$ :

$$A = \begin{pmatrix} d_1 & & U \\ & \ddots & \\ L & & d_N \end{pmatrix} \quad (4.5)$$

The upper part  $U := (a_{ij})_{i < j}$  of  $A := (a_{ij})_{i,j=1}^N$  describes the rise of the occupation number of state  $i$  due to de-excitation of state  $j$  by collisions with plasma particles. The lower part  $L := (a_{ji})_{i < j}$  stands for the increase of the occupation of state  $j$  due to excitation of state  $i$ . Finally, the diagonal elements  $(d_i)_{i=1}^N := (a_{ii})_{i=1}^N$  sum up all the losses of occupation of state  $i$  due to effects described by  $U$  and  $L$ .

The coefficients  $b_{ij}$  are

$$\begin{aligned} b_{ij} &: = \frac{A_{ji}}{v_{beam}} \geq 0, i < j \\ b_{ii} &: = -\sum_{i < j} b_{ij} \leq 0 \end{aligned} \quad (4.6)$$

with  $A_{ji}$  being the Einstein coefficients, describing spontaneous emission. The B-Matrix looks similar to the A-Matrix (4.5), but here, the lower part is zero (there is no spontaneous excitation). The upper part  $(b_{ij})_{i < j}$  stands for the occupation number transfer from state  $j$  to  $i$  due to spontaneous emission, the diagonal  $(b_{ii})_{i=1}^N$  sums up, as before, the occupation decrease of state  $i$  by the emission described in the upper part.

The definitions and consistency imply, that for both the A- and B-Matrix the sum over all elements in an arbitrary column has to be zero (lost occupation of state  $i$  has to be transferred to the sum of all other states  $j \neq i$ ).

Out of the result for occupation number densities emission (Na I (state i - state j)) can be calculated using the proportionality

$$I_{Na(i \rightarrow j)} \propto N_i \quad (4.7)$$

of the emission intensity and the occupation number of the initial state.

The main Na I emission line is the transition 3p-3s @589 nm, 589.6 nm. This is the transition observed for electron density calculation (see chapter 5). Other transitions are too weak for reasonable use in electron density evaluation (detailed analysis in [25]). Introducing the proportionality factor  $\alpha$ , the proportionality can be written as

$$\alpha \cdot I_{NaI(3p-3s)} = N_2 \quad (4.8)$$

For the electron density evaluation it is sufficient to know the normalized emission intensity. The factor  $\alpha$  is either derived by a shooting method or it is one of the fit parameters (Bayesian Ansatz).

## 4.1 Implementation of the beam attenuation modeling

The beam attenuation modeling is implemented in the FORTRAN77/shell script program *simula*, consisting of several modules. Some of these modules are also used for electron density evaluation in the FORTRAN77/shell script program *absolut* and of the diagnostic *LID*. The newer diagnostics *LIN* and *IDA* use slightly modified modules and FORTRAN95.

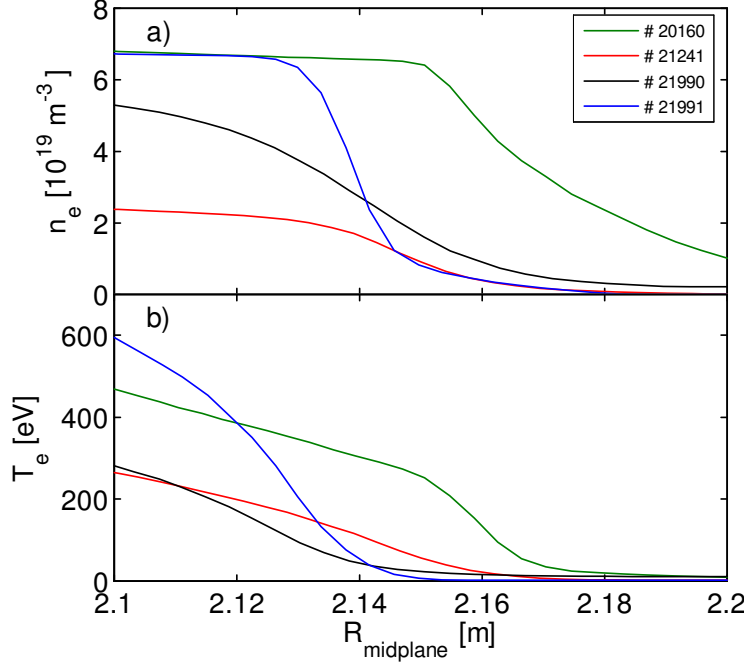


Figure 4.1: (a)  $n_e$  and (b)  $T_e$  profiles for discharges # 20160 (green), # 21241 (red), # 21990 (black), #21991 (blue) vs. midplane radius

The program `simula` consists of a shell script named `sim_na` and a compiled FORTRAN77 routine named `sim_[Eb]` ([Eb] is replaced by the beam energy in keV). In B.2 short descriptions are given and the differences to the old (Li-beam) modules are mentioned. All details are commented in the source code.

## 4.2 Examples

As examples for modeling the four following discharges ( $n_e$  and  $T_e$  profiles) were used. Two of the discharges are standard scenarios: the "Standard H-Mode" (#20160) and the "Standard ohmic" (#21241). Two discharges of the first Na campaign, where both Na and Li beam  $n_e$  evaluation was done (#21990, #21991), are also chosen. In table 4.1 details of  $n_e$  and  $T_e$  pedestal top values as well as the separatrix position is given. The table also lists the penetration depths, i.e. where the ground state is attenuated to 5%.

Figure 4.1 shows the  $n_e$  (4.1a) and  $T_e$  (4.1b) profiles for the four different discharges. The plotted data are fits to experimentally determined values (density: Lithium beam diagnostic and edge Thomson scattering diagnostic [6], temperature: ECE diagnostic [31], [32], [33] and edge Thomson scattering diagnostic) mapped to the magnetic midplane.

Figure 4.2 displays the modeled occupation number profiles (proportional to emission, see (4.7)): Fig. 4.2a. for a Li beam at 40 kV and fig. 4.2b. for a Na

AUG	$n_e^{\rho_{pol}=0.95}$	$T_e^{\rho_{pol}=0.95}$	$R_{sep}$	$\rho_{40\text{ kV}}^{Li}$	$\rho_{40\text{ kV}}^{Na}$	$\rho_{80\text{ kV}}^{Na}$
#	$10^{19}\text{ m}^{-3}$	eV	m	$\rho_{pol}$	$\rho_{pol}$	$\rho_{pol}$
20160	6.59	400	2.156	0.95	0.97	0.96
21241	2.24	220	2.145	0.80	0.85	0.83
21990	5.16	280	2.138	0.92	0.95	0.94
21991	6.70	550	2.140	0.94	0.96	0.95

Table 4.1: The discharges selected as examples with characterising parameters and modeled data: AUG #... ASDEX Upgrade discharge number,  $n_e^{\rho_{pol}=0.95}$ ,  $T_e^{\rho_{pol}=0.95}$ ...  $n_e$  and  $T_e$  pedestal top values,  $R_{sep}$ ... the separatrix position,  $\rho_{E_{beam}\text{ kV}}^X$ ... penetration depth (the poloidal radius  $\rho_{pol}$ , where the  $X = Na/Li$ -beam of energy  $E_{beam}$  is attenuated to 5%)

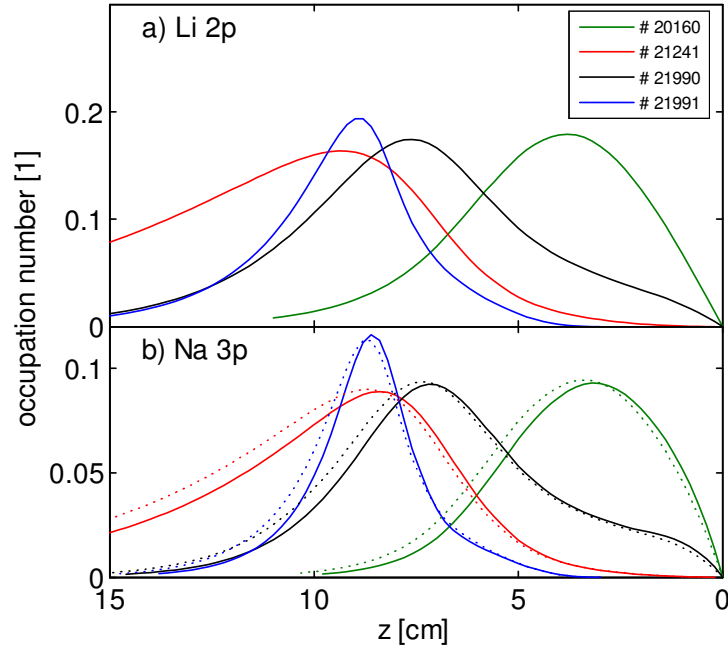


Figure 4.2: (a) Li 2p ( $E_{beam} = 40\text{ keV}$ ) and (b) Na 3p ( $E_{beam} = 40\text{ keV}$ ,  $E_{beam} = 80\text{ keV}$  dotted) occupation profiles vs. beam coordinate modeled for  $n_e$  and  $T_e$  profiles of fig. 4.1



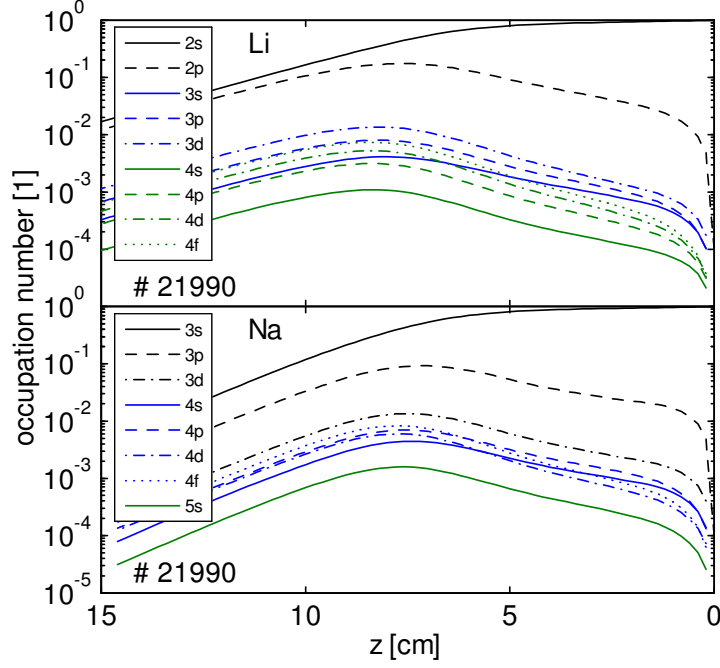


Figure 4.3: AUG # 21990: occupation number densities for the excited states taken into account.

beam at 40 and 80 keV. Therefore the profiles shown in fig. 4.1 are used as input for modeling, the plasma is assumed to be clean ( $Z_{eff} = q = 1$ ).

The main observation is that the maxima of the Na I emission profiles are only slightly shifted to the outside as compared to Li (about 2 to 3% of  $\rho_{pol}$ ). Also, the difference between a 40 keV and 80 keV Na beam is only marginal (1% of  $\rho_{pol}$ ). This is mainly due to the fact that the excited states of Na are considerably less occupied than in the case of Li and consequently the very efficient charge exchange from these states, mostly responsible for the attenuation of the beam, plays only a minor role. Especially the state Na 3p is significantly less occupied than Li 2p, due to its shorter lifetime (occupation in figure 4.3, lifetimes in 2.2). The penetration depth of a Na beam is thus only slightly lower than that of a Li beam at an acceleration voltage of 40 keV. For higher acceleration voltages, the penetration depth of Li increases considerably, while the one of Na hardly changes.

As can be seen later in chapter 7 the differences in the evaluation depths (as deep as the relative evaluation error stays below a certain limit) of the LIN diagnostic are in the same order as the differences in penetration depths and differences in the locations of the maxima of emission profiles.



## Chapter 5

# Calculation of electron density

The programs/diagnostics using the shooting method are based on an algebraic rearrangement of the modeling differential equation [34]. Using a boundary condition (at the point of singularity or where the beam is assumed to be completely attenuated) the factor  $\alpha$  (as defined in (4.8)) is determined by this shooting method.

### 5.1 Program absolut / shooting method

#### 5.1.1 Rearrangement of the modeling equation

The modeling equation for the occupation of the Na 3p state (2nd equation in (4.1)) is

$$\frac{dN_2}{dz} = \sum_{j=1}^N \{n_e(z) a_{2j}(T_e(z)) + b_{2j}\} N_j(z) \quad (5.1)$$

All functions are integrable, so integration over the interval  $[z, z+h]$  gives

$$N_2(z+h) - N_2(z) = \sum_{j=1}^N \int_z^{z+h} \{n_e(s) a_{2j}(T_e(s)) + b_{2j}\} N_j(s) ds$$

$n_e$  and  $N_j$  are continuous and for  $h$  small enough, such that the terms  $n_e(s) a_{2j}(T_e(s)) + b_{2j}$  and the coefficients  $a_{2j}(T_e(s))$  don't change their signs, the first mean value theorem for integration can be used giving

$$\begin{aligned}
N_2(z+h) - N_2(z) = & \left[ \sum_{j>2} hb_{2j} N_j(\zeta_j) + b_{22} \int_z^{z+h} N_2(s) ds \right] + \\
& + n_e(\zeta) \left[ \sum_{j \neq 2} \int_z^{z+h} a_{2j}(T_e(s)) ds N_j(\zeta_j) + \int_z^{z+h} a_{22}(T_e(s)) N_2(s) ds \right] \\
\zeta, \zeta_j \in & [z, z+h]
\end{aligned}$$

Algebraic rearrangement now gives (assuming the denominator being non-zero):

$$n_e(\zeta) = \frac{N_2(z+h) - N_2(z) - b_{22} \int_z^{z+h} N_2(s) ds - \sum_{j>2} hb_{2j} N_j(\zeta_j)}{\int_z^{z+h} a_{22}(T_e(s)) N_2(s) ds + \sum_{j \neq 2} \int_z^{z+h} a_{2j}(T_e(s)) ds N_j(\zeta_j)}$$

Using equation (4.8) and assuming that  $h$  is small enough such that  $n_e(\zeta) \approx n_e(z)$ ,  $N_j(\zeta_j) = N_j(z)$ ,  $\forall j \neq 2$  leads to the approximation for the electron density

$$\begin{aligned}
n_e(z) \approx & \frac{\alpha [I_{3p \rightarrow 3s}(z+h) - I_{3p \rightarrow 3s}(z)] - \alpha b_{22} \int_z^{z+h} I_{3p \rightarrow 3s}(s) ds - \sum_{j>2} hb_{2j} N_j(z)}{\alpha \int_z^{z+h} a_{22}(T_e(s)) I_{3p \rightarrow 3s}(s) ds + \sum_{j \neq 2} \int_z^{z+h} a_{2j}(T_e(s)) ds N_j(z)} \\
& (5.2)
\end{aligned}$$

### 5.1.2 The singularity condition / point of singularity

As long as the denominator in equation (5.2) doesn't change its sign,  $n_e$  can be evaluated solving (4.1) with a differential equation solver using equation (5.2). The point  $z = z_s > 0$ , where the denominator is zero, is the so-called point of singularity. The continuity and positivity of  $n_e$  proves that at  $z_s$  the nominator has also to be zero and change its sign.

A first approximation for the point of singularity can be given neglecting the lower occupied states ( $j > 2$ ) in the nominator of (5.2):

$$[I_{3p \rightarrow 3s}(z_s + h) - I_{3p \rightarrow 3s}(z_s)] + |b_{22}| \int_{z_s}^{z_s+h} I_{3p \rightarrow 3s}(s) ds = 0 \quad (5.3)$$

For  $h \rightarrow 0$  this becomes

$$\frac{dI_{3p \rightarrow 3s}}{dz}(z_s) + |b_{22}| I_{3p \rightarrow 3s}(z_s) = 0 \quad (5.4)$$

A first result is that the singularity can not occur before the maximum of the emission profile is reached, because  $\frac{dI_{3p \rightarrow 3s}}{dz}(z) > 0$  until the maximum.

For the evaluation of the electron density in an interval  $[z_0, z_L]$  it is also necessary to know the factor  $\alpha$  in (5.2).  $\alpha$  can be determined using a shooting method, because the dependence of the nominator on  $\alpha$  is much lower than the dependence of the denominator in

$$n_e(z) \approx \alpha \frac{[I_{3p \rightarrow 3s}(z+h) - I_{3p \rightarrow 3s}(z)] - b_{22} \int_z^{z+h} I_{3p \rightarrow 3s}(s) ds - \alpha^{-1} \sum_{j>2} h b_{2j} N_j(z)}{\alpha \int_z^{z+h} a_{22}(T_e(s)) I_{3p \rightarrow 3s}(s) ds + \sum_{j \neq 2} \int_z^{z+h} a_{2j}(T_e(s)) ds N_j(z)} \quad (5.5)$$

which is equivalent to (5.2). Depending on whether  $z_s$  lies inside or outside the interval  $[z_0, z_L]$  a different boundary condition has to be applied for determining  $\alpha$  in the shooting method.

In the first case,  $z_s \in [z_0, z_L]$ , it is shot for  $\alpha$  such that the denominator is zero at  $z = z_s$  (boundary condition in this case).

In the second case, when no singularity occurs in the evaluation interval, the boundary condition is  $N_1(z_{end}) = 0$ . This means that the ground state is fully attenuated. Usually  $z_{end}$  is chosen as the point, where  $I_{3p \rightarrow 3s}$  has fallen to 0.1% of its maximal value.

For some low density regimes, where neither the singularity occurs nor the ground state is enough attenuated at the inner border of the observed interval, it is not possible to obtain an electron density profile with this method.

Because  $\alpha$  is determined by the shooting method, it is not necessary to know the absolute emission values, only the relative, normalized emission profiles are needed. This simplifies the calibration of the optical channels, only relative calibration has to be done.

### 5.1.3 Implementation of the program absolut

The structure of the implementation is very similar to the implementation of the modeling in the program `simula`. The program `absolut` consists of a shell script `abs` and a FORTRAN77 program with compiled name `abs_[Ebeam]`. Some of the FORTRAN77 modules are also used in `simula` and were already described in B.2. Some other functions and subroutines are also the same or similar in both programs, but are in different modules / files. Again an overview is given in B.3 with focus on changes that were done. All details are commented within the source code.

## 5.2 Diagnostic LID / shooting method

The diagnostic LID uses the same algorithm as the program `absolut`. But there are several additional routines, mainly for input/output. These routines read in the raw data (diagnostic LIB) of the 35 channels of the upper optics and prepare the data for the shooting method, for instance the background (signal

when beam is off) is subtracted and the data is averaged over some emission profiles. The output routines write the  $n_e$  data directly into the shotfile.

The changes between the (old) Lithium version and the version for the sodium beam were mainly the same as described for the program absolut. Additionally the beam coordinates had to be adapted due to the different refraction in the optics (see 2.2.1).

### 5.3 Diagnostic LIN / Bayesian Ansatz

A detailed description of the Diagnostic LIN using the Bayesian Ansatz can be found in [35] (Probabilistic lithium beam data analysis).

Here a short summary will be given. A description of all program changes being necessary due to the use of Na instead of Li is located in B.4.

In general, it is not possible to solve for the electron density profile uniquely using the discrete 35 spatial data points deteriorated by noise and dependent on calibration data that also contains uncertainties. In the old method these problems are solved by making a smooth function out of the discrete data points. Then this smooth function is used in the shooting method. One of the disadvantages of this approach is that information about noise and error is lost.

All these errors and estimates can be taken into account using Bayesian probability theory (BPT). This theory is applied in diverse fields of plasma physics, physics and science in general. The Bayes formula reads as follows:

$$P(A|B) = \frac{P(B|A)P(A)}{P(B)}$$

For electron density  $n_e$  evaluation using data  $d$  with noise  $\sigma$  and additional information about the problem  $I$  the starting equation reads

$$P(n_e|d, \sigma, I) = \frac{P(d|n_e, \sigma, I) P(n_e|I)}{P(d|I)}$$

or simplified

$$P(n_e|d) = \frac{P(d|n_e) P(n_e)}{P(d)}$$

This looks like the simple Bayes formula, but here we deal with probability densities instead of probabilities. In detail it looks like that:

$$f_{N_e, Z}(n_e, z|D = d) = \frac{f_{N_e, Z, D}(n_e, z, d)}{f_D(d)} = \frac{f_D(d|N_e = n_e, Z = z) f_{N_e, Z}(n_e, z)}{f_D(d)}$$

with the denominator

$$f_D(d) = \int_{\Omega} f_D(d|N_e = \nu_e, Z = \zeta) f_{N_e, Z}(\nu_e, \zeta) d\nu d\zeta$$

that is only used for normalization.

So the posterior function  $f_{N_e, Z}(n_e, z|D = d, \sigma, I)$  is proportional to the product of the prior function  $f_{N_e, Z}(n_e, z|I)$  times the likelihood function  $f_D(d|N_e = n_e, Z = z, \sigma, I)$ .

For the Li- / Na-beam intensity data set ( $N_s = 35$  spatial channels and  $N_t$  time frames, recorded every  $50 \mu s$ ) the combined likelihood function of  $N_d = N_s \cdot N_t$  data values is given by

$$f_D(d|N_e = n_e, Z = z, \sigma, I) = \prod_{i,j}^{N_s, N_t} \frac{1}{\sqrt{2\pi}\sigma_{ij}} \exp \left[ \underbrace{\left( \frac{d_{ij} - D_i(n_e)}{\sigma_{ij}} \right)^2}_{\chi^2 := \sum_{i,j} (\dots)^2} \right] \quad (5.6)$$

This is the product of Gaussian likelihood functions because of the independent and normally distributed errors  $\epsilon_{ij} = d_{ij} - D_i(n_e) \sim N(0, \sigma^2)$ . The modeled intensity data  $D$  is given by

$$D_i(n_e) = I_i = \alpha s_i N_2(n_e(z_i))$$

Additionally the estimated background (measured during beam-off periods and containing essential information) has to be considered, resulting in

$$\epsilon_{ij} = d_{ij} - (D_i + D_{i,b})$$

where the subscript  $b$  stands for "background". The error in background determination is defined in the same way as the error of intensity data:  $\epsilon_{ij,b} = d_{ij,b} - D_{i,b} \sim N(0, \sigma_b^2)$ .

After adding the variance  $\Delta s_i^2$  of the calibration constant  $s_i$  the modified  $\chi^2$ -term in (5.6) can be written as

$$\chi^2 = \sum_{i,j}^{N_d} \frac{(d_{ij} - d_{ij,b} - D_i(n_e))^2}{\sigma_{ij}^2 + \sigma_{ij,b}^2 + \left( D_i(n_e) \frac{\Delta s_i}{s_i} \right)^2}$$

The prior function contains the prior information, that the density profile is almost monotonically decreasing from plasma core to edge. It contains a Gaussian penalization term with regularization parameter  $s_g$ . The higher  $s_g$  is, the more we believe in monotonicity. There is also a second prior function that penalizes the density profile curvature, using a parameter  $s_c$ . Too high  $s_c$  cause oversmoothed profiles, while too low  $s_c$  facilitates noise fitting.

Error bars, reflecting the quality and accuracy of the derived profile, are also provided. The calculation of these error bars is not trivial, because the  $n_e$  evaluation is a non-local interpretation of the measurements. The electron density and also its error at a certain spatial position is not only depending on the obtained emission profile at this position, but also on the plasma the beam has already passed. Additionally constraints and prior informations have an influence. Therefore, for further calculations using the derived  $n_e$  profiles, it is recommended to use the full posterior pdf as prior pdf for the following analysis. For the error bar calculation it is sufficient to use the following method that is commonly used by the diagnostic LIN:  $n_e$  values are increased/decreased such that the misfit  $\chi^2$  is increased by  $\Delta\chi^2 = 1$ .

In the implementation the density profiles are represented as exponential of cubic splines. Typically 14 parameters (13 spline parameters and  $\alpha$ ) are optimized, and the solver of the system of coupled linear differential equations is the most time consuming part. The numerical effort is comparable to the conventional analysis (LID) for a single time slice.

## 5.4 Diagnostic IDA / integrated data analysis with Bayesian Ansatz

The diagnostic IDA relies on the same method as the diagnostic LIN, but as additional input values the interferometer channels H1 to H5 are used [36]. These five channels provide line integrated  $n_e$  data at 5 positions between the ETB zone and the plasma core. This enables the evaluation of  $n_e$  on the full scale from plasma center ( $\rho_{pol} = 0$ ) over the ETB zone and the separatrix ( $\rho_{pol} = 1$ ) to the Scrape off layer ( $\rho_{pol} > 1$ ). In future this method is intended to be extended on combining the data sets of even more diagnostics at ASDEX Upgrade. For  $n_e$  evaluation the inclusion of the Thomson Scattering diagnostic [6], [7] and the Reflectometry [8], [9], [17] data could increase the accuracy. The more diagnostics are included, the higher is the numerical effort, because of increasing data and parameter set sizes. So for the IDA diagnostic the computation time rises by one order of magnitude as compared to the LIN diagnostic, but is still acceptable.

As the LIN diagnostic the error bars given by the diagnostic IDA enable comparing the errors to other diagnostics as Edge Thomson Scattering. There is no smoothing like in the conventional data analysis method that leads to a loss of error information.



## Chapter 6

# Dependence on secondary input data

The evaluation of  $n_e$  profiles depends mainly on the line emission data recorded by the optics. But there are also other parameters that influence the calculations: The (electron) temperature and the impurity ion density. Both have a direct effect on the collisional rates (the A-matrix, (4.3)). Because no immediately available and exact data is offered for both electron temperature and impurity ion density profiles, the effect of inaccuracies and the use of a few typical profiles selected by discharge type instead of individual ones has to be analyzed.

### 6.1 Dependence on electron temperature ( $T_e$ ) profiles

$T_e$  profiles are not immediately available during routine plasma operation. Therefore after classification of the discharge, a typical  $T_e$  profile is taken as input for  $n_e$  evaluation. One possibility to describe such a typical profile is a tanh-shaped curve in the region of interest, the edge transport barrier (ETB) zone. In this case four parameters define the  $T_e$  profile: the separatrix position, where the temperature is set to  $T_e^{sep} = 100$  eV, the scrape off layer (SOL) and pedestal top temperatures  $T_e^{SOL}$ ,  $T_e^{ped}$  and the width of the pedestal, varying in the range of several cm. Generally the separatrix position is well determined, while the SOL temperature is not and can range from 5 – 20 eV. The pedestal top temperature and the pedestal width depends on the discharge type (L-mode, H-Mode) and heating power.

A short view on the reduced rates (see 3s electron loss and 3s-3p excitation rates in fig. 6.1) let us expect, that in the area between 10 and 1000 eV, the temperature dependence is very low.

To verify this expectation, two tests for dependence of  $n_e$  evaluation on realistic uncertainties in  $T_e$  profiles were done:

**SOL temperature** As mentioned above, the SOL electron temperature is not well determined. So the influence of variations of  $T_e$  for  $\rho_{pol} > 1$  was tested by keeping the  $T_e$  profile constant for  $\rho_{pol} < 1$  and for  $\rho_{pol} > 1$  the SOL

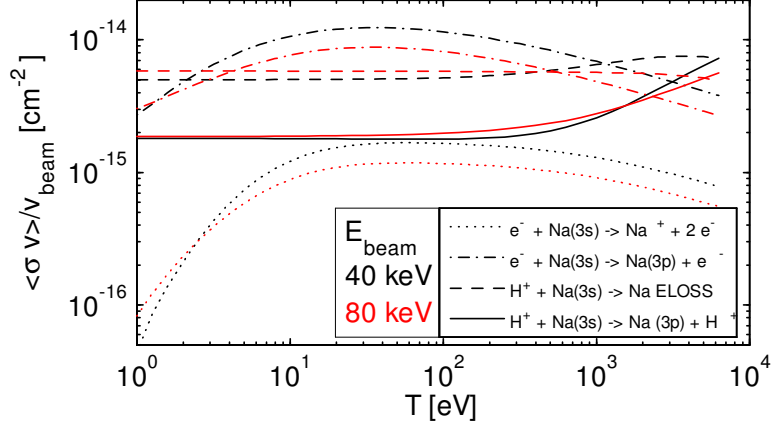


Figure 6.1: Reduced rates for collisions of electrons and protons with Na. black:  $E_{beam} = 40 \text{ keV}$ , red:  $E_{beam} = 80 \text{ keV}$ .

temperature ( $T_e^{SOL}$ ) was set to fixed values out of  $\{2, 5, 10, 20, 50\}$  eV (see fig. 6.2a). As can be seen in fig. 6.2b, the reconstructed  $n_e$  profiles do not show any effect inside the separatrix position ( $\rho_{pol} = 1$ ). Outside, the most significant differences occur for  $T_e^{SOL} = 2 \text{ eV}$ , being below the excitation threshold of the Na I (3p-3s) transition. All other settings differ less than 25% (fig. 6.2c), the absolute errors are quite small (fig. 6.2b).

**pedestal width** Keeping  $T_e^{SOL} = 5 \text{ eV}$ ,  $T_e^{sep} = 100 \text{ eV}$  and  $T_e^{ped} = 800 \text{ eV}$ , the width of the pedestal is varied between 10 and 80 mm (see fig. 6.3a). As can be seen in fig. 6.3b, the  $n_e$  profiles is nearly independent of these changes in the ETB zone, the area of interest. Outside the separatrix position the differences can reach, as before, 25% (fig. 6.3c), corresponding to very small absolute errors (fig. 6.3b).

Because  $n_e$  evaluation is, especially in the ETB zone, not sensitive to  $T_e$  profiles, it is sufficient to select one of two typical  $T_e$  profiles, one for H-Mode and one for L-Mode plasmas. This selection is done by a regime identification algorithm and used subsequently for  $n_e$  evaluation.

## 6.2 Dependence on $Z_{eff}$ profiles

At ASDEX Upgrade, there is no diagnostic providing  $Z_{eff}$  profiles ( $Z_{eff}$  and  $q$  data as defined in 3.2) for each individual shot. As input for  $n_e$  evaluation, reasonably realistic  $Z_{eff}$  profiles are used. These profiles have been determined using data by several impurity ion density diagnostics, like Li-CXS (LIA, LIC). As for  $T_e$  profiles above, it is clear, that the real  $Z_{eff}$  profile differs from the one used for  $n_e$  evaluation. How large the effect of this differences on the  $n_e$  profiles evaluated by the Na-IXS diagnostics are, has been researched as follows.

A reference  $n_e$  profile (black line in fig. 6.4) and  $T_e$  profile is taken as base for the calculation. Then the Na (3p-3s) emission profiles for a pure D (clean

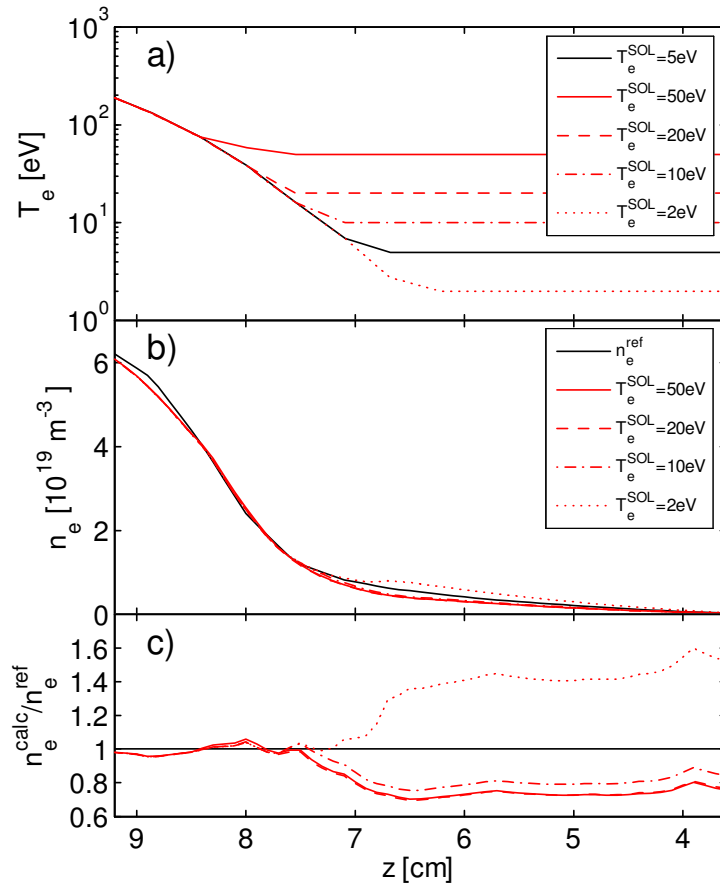


Figure 6.2: AUG # 21991: (a)  $T_e$  profile, varying  $T_e^{SOL}$ , (b)  $n_e^{calc}$  compared to  $n_e^{ref}$  (black), (c) ratio to  $n_e^{ref}$

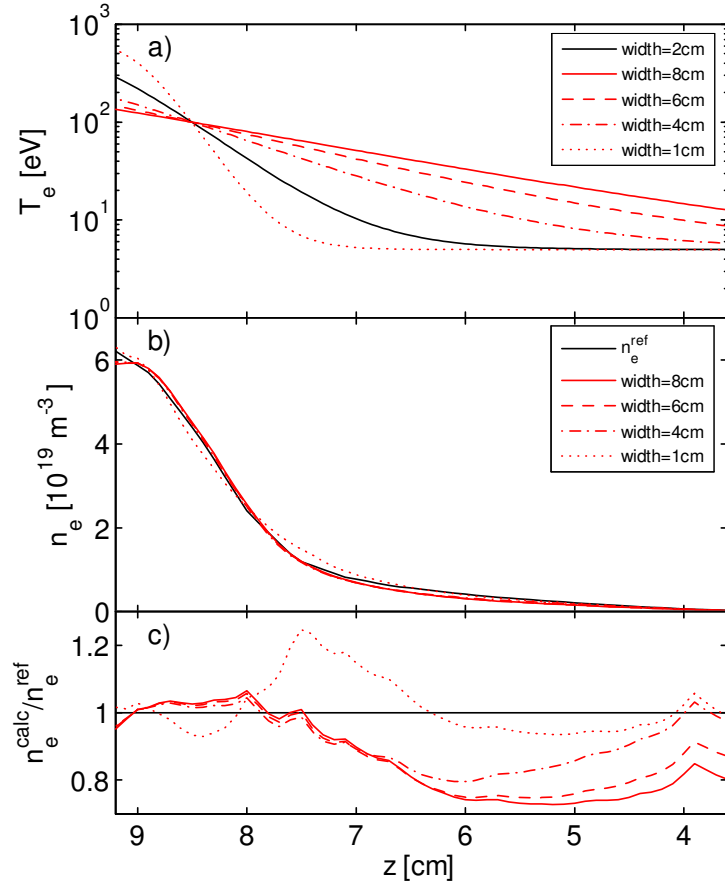


Figure 6.3: AUG # 21991: (a)  $T_e$  profile, varying width( $T_e$ -profile), (b)  $n_e^{\text{calc}}$  compared to  $n_e^{\text{ref}}$  (black), (c) ratio to  $n_e^{\text{ref}}$

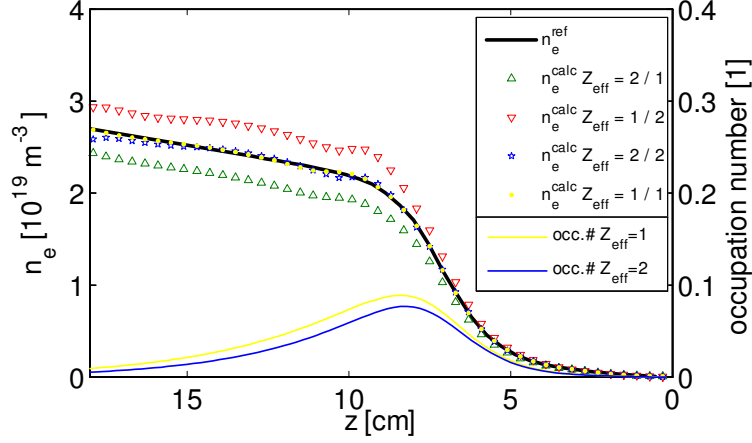


Figure 6.4: AUG #21241: left axis:  $n_e^{ref}$  (black) compared to reconstructed  $n_e$  profiles: the first index gives the species for the modeled Na 3p profile, the second for the assumption of the reconstruction: D/D (yellow dots), He/He (blue stars), D/He (red triangles), He/D (green triangles); right axis: Na 3p occupation number for D (yellow line) and He (blue line)

plasma,  $Z_{eff} = q = 1$ ) and a pure He plasma ( $Z_{eff} = q = 2$ , representing a strongly impurified plasma) are calculated by the program *simula* (yellow and blue lines / right axes in fig. 6.4).  $n_e$  evaluation of these emission profiles with the correct plasma parameters (the same as in the modeling) give the yellow and blue  $n_e$  profiles. These profiles correspond very well to the reference  $n_e$  profile. If completely false  $Z_{eff}$  profiles are used for  $n_e$  evaluation (D for modeling, He for  $n_e$  evaluation: red triangles; He for modeling, D for  $n_e$  evaluation: green triangles), the differences in  $n_e$  to  $n_e^{ref}$  are about 15%, and so for reasonably realistic profiles as used in standard application, these errors remain below 5%.



## Chapter 7

# Experimental results

Up to July 2008 three campaigns of Na beam measurements have been conducted. In the first campaign, in 2007, a Li emitter with 10% of Na was used. So the standard Li beam  $n_e$  evaluation is not disturbed, while the potential of Na is tested by the lower optics. Due to the results it was decided to run experiments with Na dominated or pure Na beam and use an appropriate upper optics. After proper filters have been purchased a mixed 9:1 Na:Li emitter was used during one week (2nd campaign). The results are comparable to the Li-beam, but the emitter lifetime was too short. So a third campaign is run with a pure Na emitter to test if a long operational time can be achieved (several weeks), the results of the second campaign can be reproduced, and what effects parameter changes (for instance higher Ebeam) have. In the last week of the third campaign a He and a H campaign are run and the capabilities of the Na beam are also tested under these conditions.

### 7.1 First campaign (Na:Li=1:9)

(from 28.6.2007 to 10.7.2007, discharges # 21967-22046)

The Li beam diagnostic is an important electron density diagnostic at AS-DEX Upgrade. Nevertheless, it has been thought about possibilities of further improvement. One of the possibilities taken into account has been the use of different elements for the neutral atom beam. Beside the use of H or He (commonly in combination with the NBI) sodium (Na) has been considered to have several advantages (see chapter 2.2). After the availability of the atomic database [1] a mixed Na-Li-emitter is built in and replaced the standard Li emitter. The mixture ratio of Na:Li=1:9 grants an undisturbed operation of the Li beam IXS diagnostic, while the Li CXS diagnostic (lower optics) is used for Na IXS measurements. A further advantage of this approach is that no filters for the Na line had to be purchased. The main disadvantages are the low Na current in the beam and the lower accuracy and spatial resolution of the lower optics. Nevertheless, it was sufficient to get first practical knowledge about the potential of a Na beam diagnostic and to test the validity of the underlying database.

A detailed analysis of the data of all plasma discharges (about 20 useful discharges within 3 weeks) in this first campaign has been done in [25]. The main results of this work are summarized below.

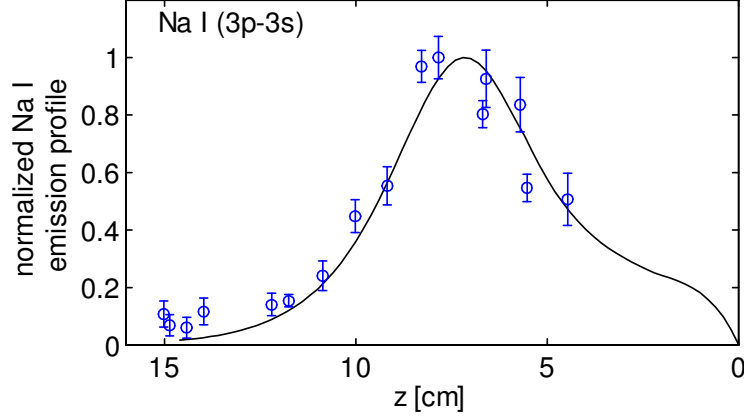


Figure 7.1: AUG # 21990: modeled emission profile (black) and measured data (blue, 18 channels)

In fig. 7.1 it is shown, that the modeled Na I (3p-3s) emission profile by simula (black line) corresponds very well to the measured Na I (3p-3s) emission (blue circles). As input for modeling, a reference electron density, derived by the Li beam and edge Thomson Scattering diagnostics, is used ( $n_e^{ref}$  in fig. 7.2). The good correspondence of the two profiles tells that the simula-program, used for modeling, contains no (significant) systematic errors. This means also that the underlying data base [1] is valid.

Fig. 7.2 shows the  $n_e$  evaluation, where the program absolut (shooting method) is used.  $n_e^{ref}$  is compared to the electron density calculated out of the measured Na I (3p-3s) emission data (blue stars) and to the electron density calculated out of the modeled emission (red dots). The  $n_e$  evaluation of the measured data despite the lower spatial resolution and bigger emission measurement errors of the lower optics shows acceptable results as compared to the reference profile. Further, the evaluation of the modeled data ensures that the  $n_e$  evaluation is the inverse process of modeling, without (significant) systematic errors within one of the two programs. The nearly negligible errors are due to the use of discrete data points, smoothing methods and rounding errors in the shooting method.

## 7.2 Second campaign (Na:Li=9:1)

(from 15.4.2008 to 17.4.2008, discharges # 23052-23092)

After the positive results of the first campaign it was decided to run a second campaign with the Na beam. Filters were purchased to use the upper optics filter-photomultiplier setup with high spatial and temporal resolution. The mixture part of Na in the emitter was increased to Na:Li=9:1. Beside the change of emitter and filters also the voltage for focusing the beam was adjusted. Further the Na-implementation of the diagnostic LID has already been finished at the start of the second campaign for an immediate availability of the evaluated data.



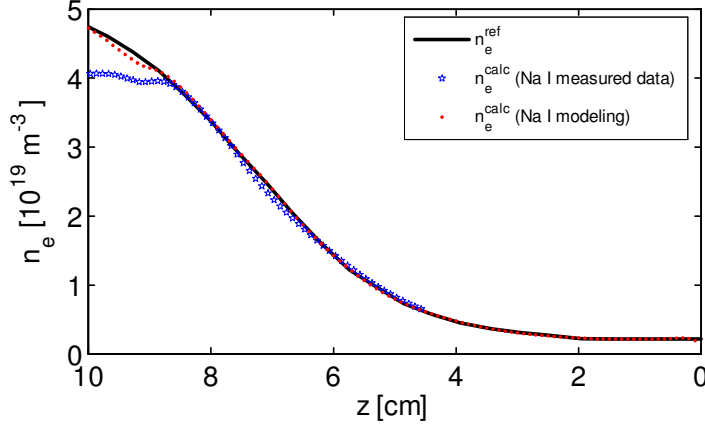


Figure 7.2: AUG # 21990:  $n_e^{ref}$  calculated of Li I measured (black),  $n_e$  calculated of Na I measured (blue),  $n_e$  calculated of Na I modeled (red)

So after fine tuning of focusing the beam in discharge # 23051, the Na-beam diagnostic measured useful Na I (3p-3s) emission data for all plasma discharges within one week (two experimental days). The measured intensity at the photomultipliers increased during the first experimental day (the emitter was heated up further), but in the end of the second experimental day the beam intensity started to decrease at constant emitter temperature. Tests next morning showed that the emitter emission has changed from Na to Li, such that with this emitter it was not possible any more to produce a Na beam of sufficient intensity. So the lifetime of this one mixed emitter was too low, but the results within these two experimental days were promising (see 7.2.1-7.2.3).

### 7.2.1 Standard H-Mode discharges

The "Standard H-Mode" is a standardized discharge type periodically done at ASDEX Upgrade. It is done practically every experimental day as first plasma discharge. This allows to compare the performance of the Na and Li beam diagnostic under the same plasma conditions in H-Mode plasmas.

In the second Na campaign discharge #23074 was of this type. A time trace of the plasma edge electron density by IDA for this discharge is shown in fig. 7.3. For comparison to the Li beam the discharges #23041 (with the Li emitter used before the Na campaign) and #23300 (with a rather new Li emitter) are taken. The regarded interval is  $t \in [1.5, 3] s$ , which lies for these 3 Standard H-Mode discharges within the flattop.

In table 7.1 some important plasma parameters (the electron density at pedestal top  $n_e^{\rho_{pol}=0.95}$  and the separatrix position at the Na beam  $R_{sep}$ ) and the evaluation depth of the diagnostic LIN are shown. For each point of the evaluated electron density profile the diagnostic LIN also delivers an electron density error bar (described in 5.3). At the separatrix position this error is for both Li and Na beam in the region of about 10%. Deeper inside the plasma (lower normalized poloidal radius  $\rho_{pol}$ ), this error is rising. Therefore one way of

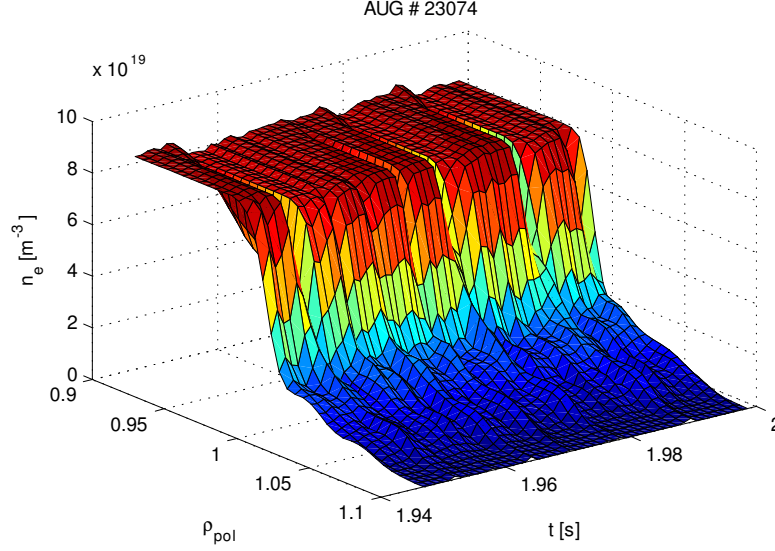


Figure 7.3: AUG # 23074 "Standard H-Mode": time trace of the edge electron density profile taken by the diagnostic IDA

AUG	beam	current	$n_e^{\rho_{pol}=0.95}$	$R_{sep}$	evaluation depth (LIN)	
#		mA	$10^{19} \text{ m}^{-3}$	m	$\rho_{pol}$ <i>error</i> < 20%	$\rho_{pol}$ <i>error</i> < 50%
23041	Li	1.7	7.5	2.130	0.959	0.937
23074	Na	2.4	7.9	2.128	0.960	0.948
23300	Li	2.8	6.9	2.132	0.942	0.919

Table 7.1: Standard H-Mode discharges with characterising parameters and data: AUG #... ASDEX Upgrade discharge number, beam... beam type (Na/Li), current... beam current,  $n_e^{\rho_{pol}=0.95}$ ...  $n_e$  pedestal top value,  $R_{sep}$ ... the separatrix position, evaluation depth (LIN)... the poloidal radius  $\rho_{pol}$  up to that the LIN evaluation error stays below the given percentage (20% or 50%).

comparing the depth of qualified evaluation (for different discharges and between Li and Na) is to define the evaluation depth as that radial position, where the error bars exceed a certain relative error (for instance 20% or 50%). Up to this evaluation depth the error remains below this border and the electron density profile can be considered to be of good quality outside this radial position.

The emitter used before the Na campaign is already weak in discharge # 23041 and so the beam intensity is lower than in discharge # 23300, where a new Li emitter is used. The Na beam shows approximately the same evaluation depth as the weak Li beam. However, the Li beam with an optimal emitter meeting a slightly lower electron density allows  $n_e$  evaluations about 2 to 3 % of  $\rho_{pol}$  deeper into the plasma.

Another possibility to compare the performance of Na and Li beams is to plot the absolute evaluation error of the IDA diagnostic over density in a scatter plot as shown in fig 7.4. Therefore all data points lying within a certain temporal

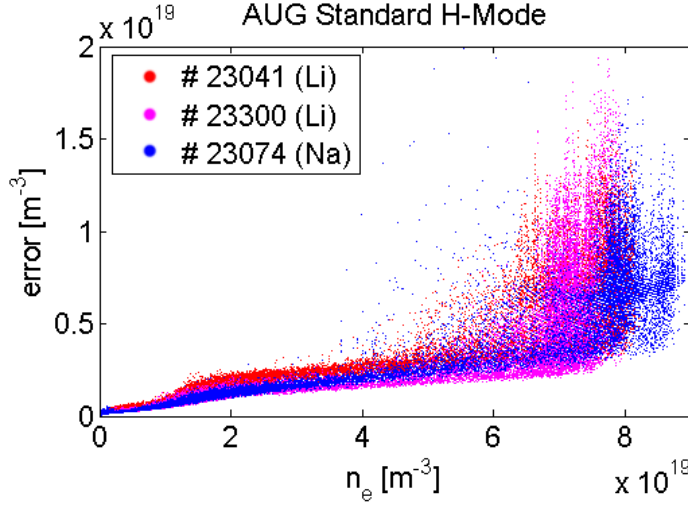


Figure 7.4: Diagnostic IDA: error bars over electron density for AUG # 23041 (red, Li beam), 23074 (blue, Na beam) and 23300 (magenta, Li beam). Radial position:  $0.92 < \rho_{pol} < 1.1$ ,  $t = [1.5, 3]$  s

and spatial interval are put into a set, and each of its members is plotted as point at its density value and absolute density evaluation error value.

Plotting the relative error over the electron density in a scatter plot (fig. 7.5) shows that up to the pedestal top densities (about  $7$  to  $9 \cdot 10^{19} \text{ m}^{-3}$ ) the error bars stay in the region of about 10% for all 3 compared discharges. This implies that the IDA diagnostic is able to produce a full range electron density profile, the Li beam penetrates far enough into the plasma to leave no missing link to the interferometer channel H5.

In general, this statement also holds for the Na beam. But as can be seen in the figures 7.4, 7.5 in the region of  $4 \cdot 10^{19} \text{ m}^{-3} < n_e < 6 \cdot 10^{19} \text{ m}^{-3}$  some single points of larger error bars occur in the case of Na, but not for the Li beam. Further investigations show that the error bars for this density region are rising during ELMs. The electron density released from the pedestal top during an ELM attenuates the beam stronger, so that the penetration depth is slightly reduced. This causes the rise of the relative error bars in the ETB zone at  $n_e \approx 5 \cdot 10^{19} \text{ m}^{-3}$  by a factor of 2 or 3, depending on the ELM, to approximately the value of 15 to 25%. This is the same level as reached by the interferometer channels H1 to H5 providing the electron density data further inside the plasma.

This effect is resolved in fig 7.6, where the electron density profile during an ELM ( $t = 1.990\text{s}$ ) and immediately afterwards ( $t = 1.991\text{s}$ ) are compared. The relative error in the ETB zone is higher during the ELM.

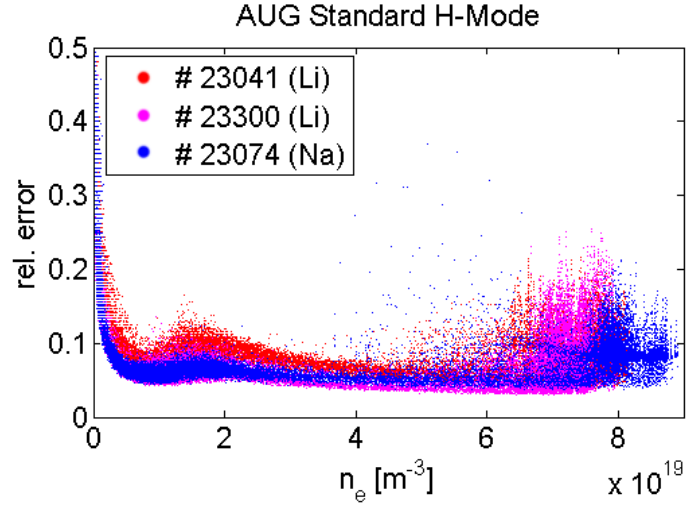


Figure 7.5: Diagnostic IDA: relative error over electron density for AUG # 23041 (red, Li beam), 23074 (blue, Na beam) and 23300 (magenta, Li beam). Radial position:  $0.92 < \rho_{pol} < 1.1$ ,  $t = [1.5, 3]$  s

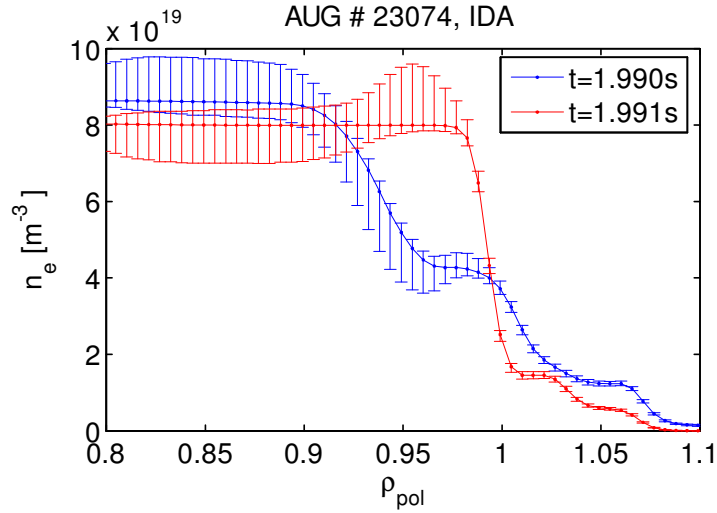


Figure 7.6: electron density profiles during an ELM (blue) and immediately afterwards (red) for AUG # 23074, IDA, Na beam

AUG	beam	VTA	$n_e^{\rho_{pol}=0.95}$	$R_{sep}$	evaluation depth (LIN) $\rho_{pol}$	
#		pos.	$10^{19} \text{ m}^{-3}$	m	$error < 20\%$	$error < 50\%$
23020	Li	edge	6.7	2.126	0.938	0.912
23021	Li	core	6.5	2.123	0.942	0.914
23065	Na	edge	6.9	2.129	0.945	0.930

Table 7.2: Improved H-Mode discharges with characterising parameters and data: AUG #... ASDEX Upgrade discharge number, beam... beam type (Na/Li), VTA pos... position of the Thomson Scattering diagnostic (edge/core),  $n_e^{\rho_{pol}=0.95}$ ...  $n_e$  pedestal top value,  $R_{sep}$ ... the separatrix position, evaluation depth (LIN)... the poloidal radius  $\rho_{pol}$  up to that the LIN evaluation error stays below the given percentage (20% or 50%).

### 7.2.2 Na beam compared to Edge Thomson Scattering and Li beam diagnostics in Improved H-Mode discharges

One of the H-Mode discharges of the second campaign with measurements of both Na beam and Edge Thomson scattering diagnostic is # 23065 (Improved H-Mode with pellets). This data is compared to the Li beam and Thomson scattering data of discharges # 23020 and # 23021 (Pedestal studies in Improved H-Mode), having almost the same plasma parameters (23065 is a repeat of 23021 and 23021 is a repeat of 23020, parameters and evaluation depth are listed in table 7.2).

Figure 7.7 shows the  $n_e$  profiles by diagnostics LIN and VTA for discharge 23065 in the time span of 2.7 to 3.0 s. For the Edge Thomson scattering diagnostics  $\rho_{pol}$  is shifted by 0.015 (= 1.5%). This shift value is derived by comparing the Edge Thomson scattering  $T_e$  profile to the ECE diagnostic. So figure 7.7 proves that the Na beam diagnostic is well corresponding to another, independent  $n_e$  diagnostic, namely the Edge Thomson scattering.

Comparing not only the profiles, but also watching the error bars is done in fig. 7.8, a scatter plot for the error bars of the values shown in fig. 7.7. The higher accuracy of the Na beam diagnostic (LIN) is obvious. The plots for the discharge 23020 (Li beam/Edge Thomson) show a similar behavior. Regarding the error bars of these different diagnostics one has to be aware of that the error determination methods are not the same. In 5.3 it is described how the LIN error bars are determined, for VTA see [7].

As for the Standard H-Mode before, comparing Na and Li beam by scatter plots was also done for these Improved H-Mode discharges, as can be seen in fig. 7.9. Here the result is the same as in 7.2.1, the accuracy of the Na beam is slightly better than the one for the Li emitter at the end of its lifetime. The cloud of points of larger error bars occurs only for the Na beam and corresponds to profiles during ELMs, this is also the same result as for the Standard H-Mode in 7.2.1.

### 7.2.3 L-Mode discharges

In the case of L-Mode discharges (low confinement) the electron density is rather low, so that no evaluation problems (using the new probabilistic algorithm) and

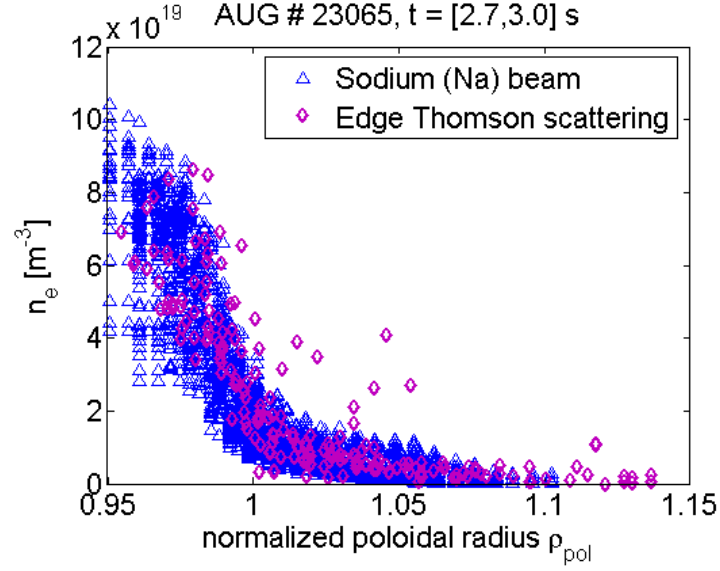


Figure 7.7: AUG # 23065: electron density profiles by Sodium beam diagnostic (LIN, blue) compared to Edge Thomson scattering diagnostic (VTA, purple) in the ETB zone.

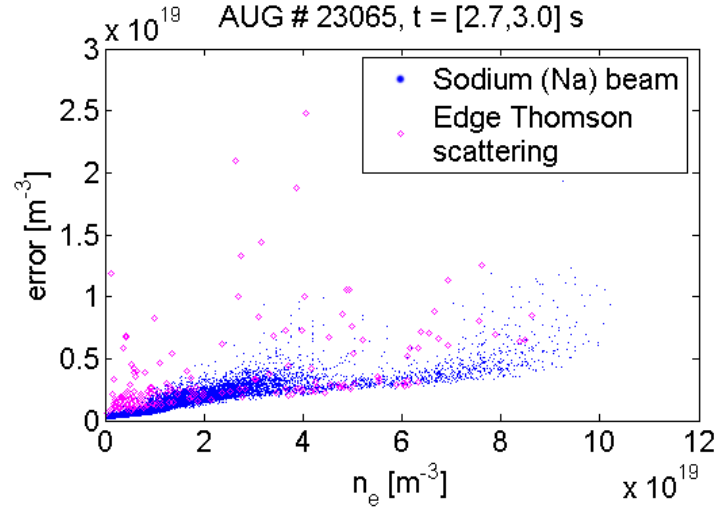


Figure 7.8: AUG # 23065: error over density for the data points shown in fig. 7.7: Na beam diagnostic LIN (blue) and Edge Thomson Scattering VTA (purple). The determination method for the error bars is not the same for the diagnostics LIN and VTA.

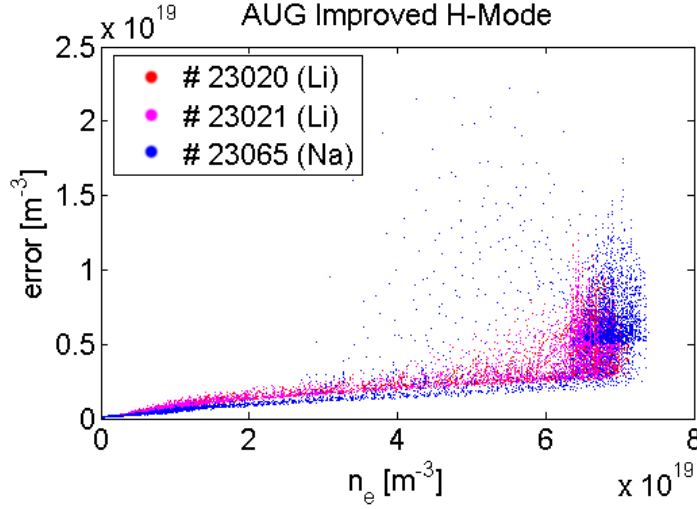


Figure 7.9: error over electron density (scatter plot) for "Improved H-Mode" discharges at ASDEX Upgrade evaluated by Na and Li beam diagnostics (IDA). Radial position:  $0.92 < \rho_{pol} < 1.1$ ,  $t = [2.7, 3]$  s

AUG #	beam	$n_e^{\rho_{pol}=0.95}$	$R_{sep}$	evaluation depth (LIN) $\rho_{pol}$	
		$10^{19} \text{ m}^{-3}$		$error < 20\%$	$error < 25\%$
23027	Li	2.8	2.099	0.979	0.969
23085	Na	2.7	2.103	0.950	0.945

Table 7.3: L-Mode discharges with characterising parameters and data: AUG #... ASDEX Upgrade discharge number, beam... beam type (Na/Li),  $n_e^{\rho_{pol}=0.95}$ ...  $n_e$  pedestal top value,  $R_{sep}$ ... the separatrix position, evaluation depth (LIN)... the poloidal radius  $\rho_{pol}$  up to that the LIN evaluation error stays below the given percentage (20% or 50%).

a high penetration depth for both Na and Li beams are expected. And there is only a small number of L-Mode discharges at ASDEX Upgrade as compared to H-Mode plasmas. Nevertheless it is also important to compare the Na and Li beam capabilities in this area.

This is done using the example of AUG # 23027 (Li beam) and its repeat AUG # 23085 (Na beam), both discharges were done for research of "ICRH W sputtering". The mean electron density in the regarded time interval  $[1.5, 2.7]$  s is about  $n_e = 4 \cdot 10^{19} \text{ m}^{-3}$ .

Typical edge plasma electron density profiles for L-Mode discharges are shown in figures 7.10, 7.11, provided by the Li and Na beam diagnostics. Here it can be talked of an excellent agreement in electron density between the two repeated discharges. As can be seen on the error bars, the evaluation depth of the Na beam is slightly better than of the Li beam. This is also shown in table 7.3, where the main plasma edge parameters are listed.

Regarding the error over density, for both IDA (fig. 7.12, showing abs. error) and LIN (fig. 7.13, showing rel. error) the Na beam delivers a slightly higher

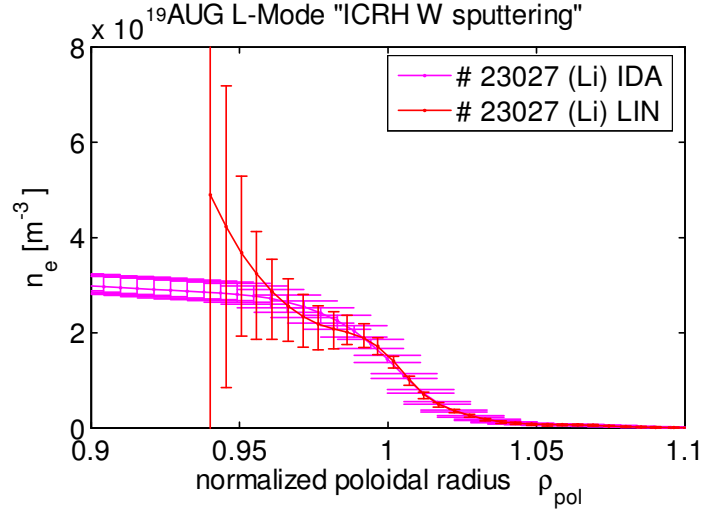


Figure 7.10: electron density profiles for AUG # 23027 by Li beam diagnostics IDA and LIN,  $t = 1.9$  s

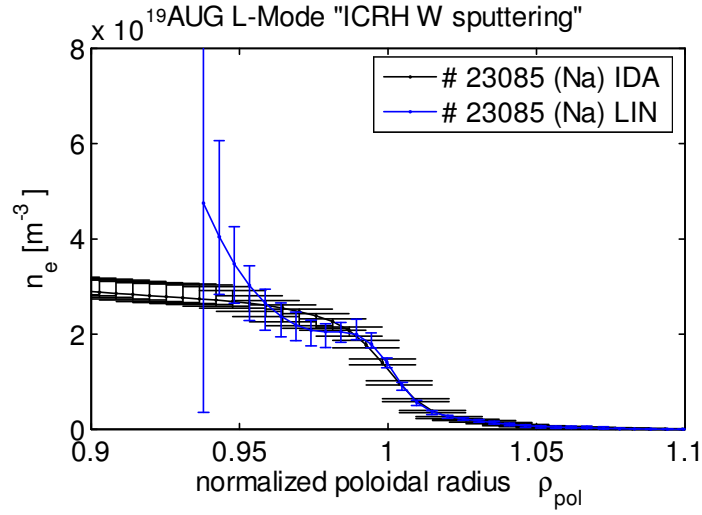


Figure 7.11: electron density profiles for AUG # 23085 by Na beam diagnostics IDA and LIN,  $t = 1.9$  s



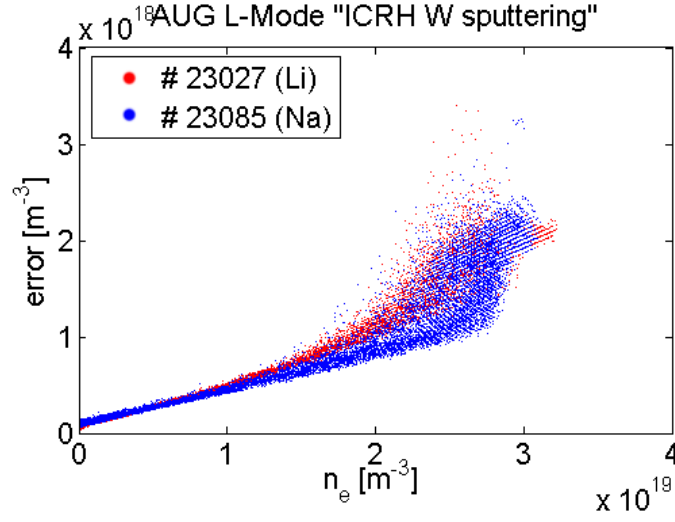


Figure 7.12: error over electron density (scatter plot) for L-Mode discharges at ASDEX Upgrade evaluated by Na and Li beam diagnostics (IDA). Radial position:  $0.92 < \rho_{pol} < 1.1$ ,  $t = [1.5, 2.7]$  s

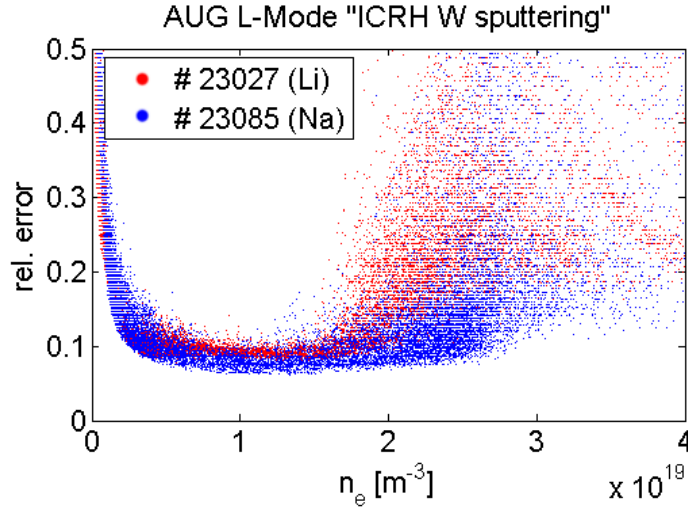


Figure 7.13: relative error over electron density (scatter plot) for L-Mode discharges at ASDEX Upgrade evaluated by Na and Li beam diagnostics (LIN). Radial position:  $0.95 < \rho_{pol} < 1.1$ ,  $t = [1.5, 2.7]$  s

AUG #	beam	current mA	$n_e^{\rho_{pol}=0.95}$ $10^{19} \text{ m}^{-3}$	$R_{sep}$ m	evaluation depth (LIN) $\rho_{pol}$	
					<i>error</i> < 20%	<i>error</i> < 50%
23074	Na	2.4	7.9	2.128	0.960	0.948
23406	Na	2.4	7.4	2.125	0.996	0.974
23429	Na	2.4	7.4	2.116	0.980	0.962

Table 7.4: Standard H-Mode discharges with characterising parameters and data: AUG #... ASDEX Upgrade discharge number, beam... beam type (Na/Li), current... beam current,  $n_e^{\rho_{pol}=0.95}$  ...  $n_e$  pedestal top value,  $R_{sep}$ ... the separatrix position, evaluation depth (LIN)... the poloidal radius  $\rho_{pol}$  up to that the LIN evaluation error stays below the given percentage (20% or 50%).

evaluation quality. For the Na beam, no negative effects of the thermal Na diffusing from the neutralization cell into the SOL area can be seen, the density and error values remain practically the same for both beam types.

Concerning L-Mode discharges it has to be mentioned that in some cases there have been problems with the old evaluation algorithm using the shooting method with singularity condition. Sometimes the singularity lies too far inside the plasma and no other boundary conditions can be used. These problems do not occur in the new probabilistic evaluation algorithm [35] that is mainly used in this work.

### 7.3 Third campaign (pure Na)

(D from 24.6.2008 to 10.7.2008, discharges # 23406-23574,

He at 11./15.7.2008, discharges # 23576-23627,

H at 17.7.2008, discharges # 23635-23654)

After the campaigns with mixed emitters the first pure Na emitter (this means a  $\text{NaAlSiO}_4$  cathode) is used in the third campaign. One aim has been to show that a much longer lifetime, as compared to the mixed Na emitter used in the second campaign, and comparable to the standardly used Li emitters, can be achieved. Further higher beam acceleration voltages are investigated. And in the last two weeks before the vessel opening of ASDEX Upgrade in Summer 2008 a He and a H campaign are driven. Herein the compatibility of the Na beam to He or H discharges is tested.

#### 7.3.1 Standard H-Mode discharges

The easiest way to compare the emitter used in the second campaign with the one of this campaign was again the Standard H-Mode discharge. Figure 7.14 shows that there are, as expected, no big differences in the IDA error bars. Additionally regarding the LIB signals (emitted Na(3p-3s) photons), beam current, penetration depths (table 7.4) and the electron density profiles let assume that there are no significant differences in between the Na beam capabilities of the emitter of the 2nd and the emitter of the 3rd Na campaign.

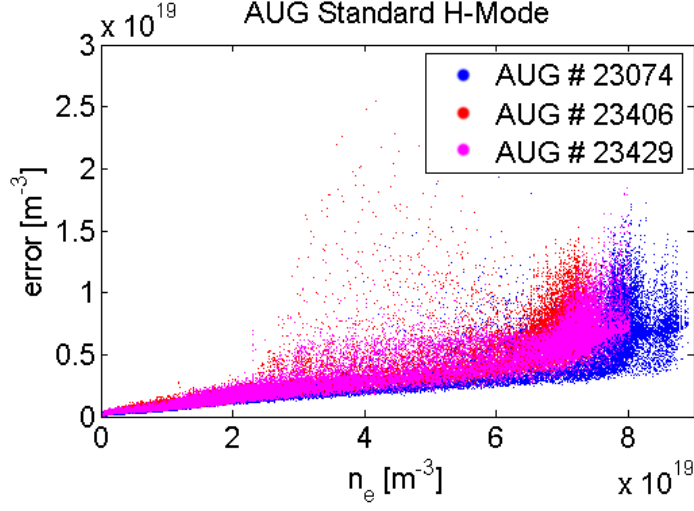


Figure 7.14: error over electron density (scatter plot) for Standard H-Mode discharges at ASDEX Upgrade evaluated by Na beam diagnostic (IDA), comparing 2nd and 3rd Na beam campaign. Radial position:  $0.92 < \rho_{pol} < 1.1$ ,  $t = [1.5, 4]$  s

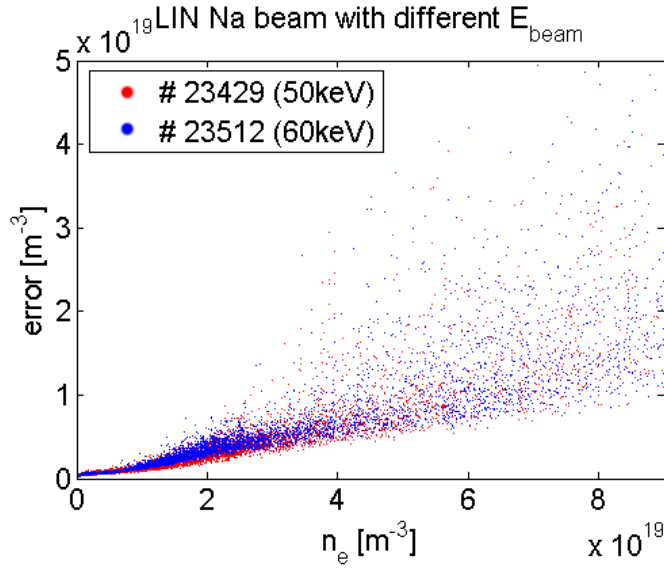


Figure 7.15: Diagnostic LIN: error bars over electron density for AUG # 23429 (blue, Na beam 50keV) and 23512 (red, Na beam 60keV).  $0.92 < \rho_{pol} < 1.1$ ,  $t = [2.5, 3]$  s

AUG	$E_{beam}$	current	$n_e^{\rho_{pol}=0.95}$	$R_{sep}$	evaluation depth (LIN) $\rho_{pol}$	
#	keV	mA	$10^{19} \text{ m}^{-3}$	m	<i>error</i> < 20%	<i>error</i> < 50%
23429	50	2.4	7.4	2.116	0.980	0.962
23512	60	1.7	8.1	2.127	0.979	0.956

Table 7.5: Comparison of different Na beam energies: Standard H-Mode discharges with characterising parameters and data: AUG # ... ASDEX Upgrade discharge number,  $E_{beam}$  ... beam energy in keV, current ... beam current,  $n_e^{\rho_{pol}=0.95}$  ...  $n_e$  pedestal top value,  $R_{sep}$  ... the separatrix position, evaluation depth (LIN) ... the poloidal radius  $\rho_{pol}$  up to that the LIN evaluation error stays below the given percentage (20% or 50%).

### 7.3.2 Higher beam energies

Modeling let us expect that going to higher beam energies will not increase the penetration depth very much (see 4.2). Nevertheless tests with a higher beam energy of  $60 \text{ keV}$  have been made during several experimental days to investigate what effects actually occur, for instance if the beam current in- or decreases.

The Na emitter used in the third campaign has shown a similar behavior that had already been observed for some Li emitters [5], [37]. When increasing the voltage (to  $60 \text{ keV}$ ), the heating (and so the temperature) of the emitter has to be reduced, to keep the beam stable. So only a current of 1.7 mA is achieved, while 2.4 mA are reached with  $50 \text{ keV}$  acceleration voltage. This leads to a worse signal-to-noise ratio and further to slightly larger errors for the  $n_e$  evaluation.

The main plasma parameters of the compared discharges as well as the slightly increased evaluation depth for higher beam energies is listed in table 7.5. As can be seen in fig. 7.15, the LIN errorbars in Standard H-Mode discharges remain approximately the same, they become a little bit worse, due to the lower beam current, as mentioned above.

Further systematic investigations on a larger number of Na emitters at higher voltages should show, if this emitter of the Na campaign has, as can be expected out of experience with Li emitters, a special and worse behavior at high voltages as compared to the average behavior of several Na emitters.

### 7.3.3 He campaign

Because of the strong He I line @ 587.6 nm there was the question if the Na beam diagnostic will work in He plasma discharges. Fig. 7.16 shows that the Na beam in a He campaign produces acceptable errorbars, even slightly better than the Li beam in He discharges. For the Na beam diagnostics the errors are about 1.5 times the errors for D campaigns and for the Li beam diagnostics the errors remain approximately twice the errors for D campaigns (see fig. 7.17). This error increase is mainly due to the worse signal-to-noise ratio in the emission data (see figures 7.19, 2.3).

Regarding the penetration / LIN evaluation depth for He discharges, the Na beam does not penetrate as deep as into a D plasma, but reaches approximately the same value as the Li beam for He discharges. The evaluation depth within the time interval  $t \in [3.5, 4] \text{ s}$  is shown in figure 7.18 and table 7.6.

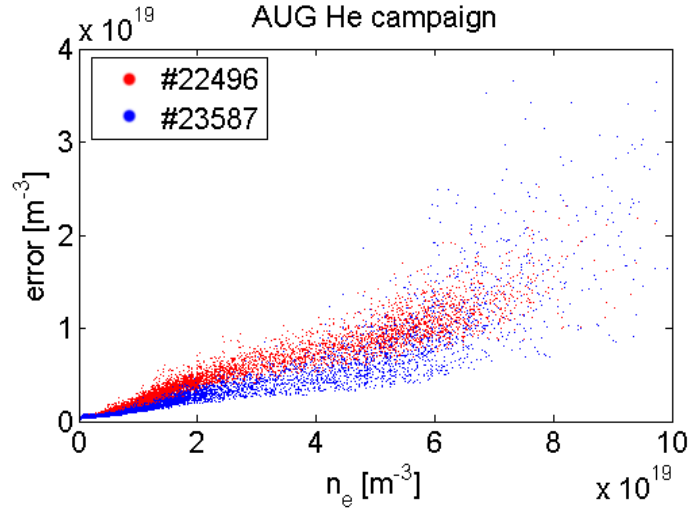


Figure 7.16: AUG He discharges: scatter plot of LIN error over electron density for  $0.95 < \rho_{pol} < 1.1$ ,  $t \in [3.5, 4]$  s

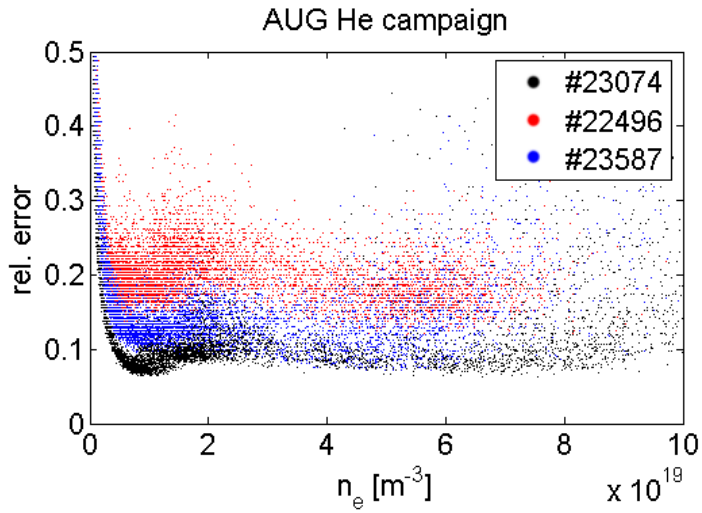


Figure 7.17: AUG He and D discharges: scatter plot of Na beam LIN error over electron density for  $0.95 < \rho_{pol} < 1.1$ ,  $t \in [3.5, 4]$  s

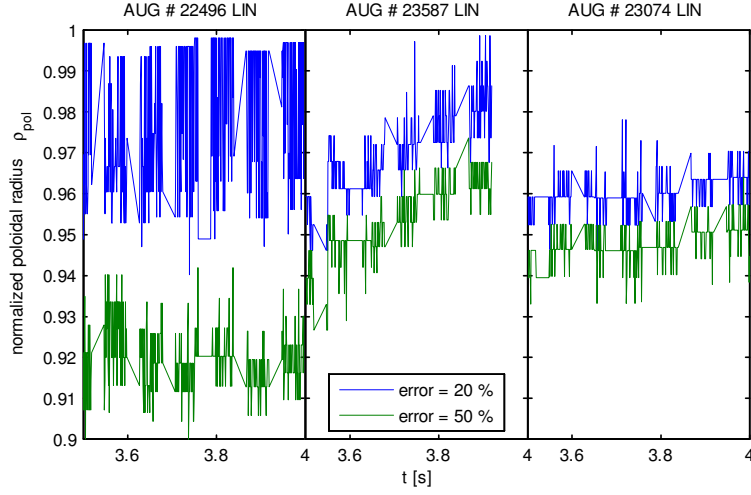


Figure 7.18: evaluation depth of diagnostic LIN in normalized poloidal radius over time for two different errorbar borders and three discharges.

AUG #	beam	plasma	$n_e^{\rho_{pol}=0.95}$	$R_{sep}$	evaluation depth (LIN) $\rho_{pol}$	
			$10^{19} \text{ m}^{-3}$		$error < 20\%$	$error < 50\%$
22496	Li	He	7.7	2.111	0.978	0.919
23074	Na	D	7.9	2.129	0.960	0.948
23587	Na	He	7.5	2.111	0.971	0.954

Table 7.6: Comparison of He and D discharges: characterising parameters and data: AUG #... ASDEX Upgrade discharge number, beam... beam type (Na/Li), plasma... plasma type (He/D/H/T/...),  $n_e^{\rho_{pol}=0.95}$ ...  $n_e$  pedestal top value,  $R_{sep}$ ... the separatrix position, evaluation depth (LIN)... the poloidal radius  $\rho_{pol}$  up to that the LIN evaluation error stays below the given percentage (20% or 50%).

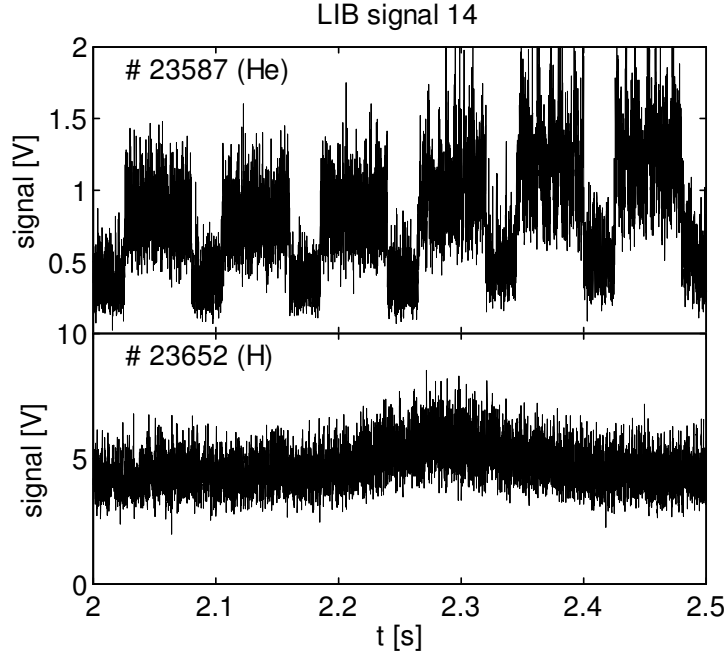


Figure 7.19: LIB signal 14 (upper optics) timetrace for a discharge in the He campaign and for one in the H campaign.

#### 7.3.4 H campaign

In H discharges also  $CH_4$  is used. This causes a very strong C II line @ 589.1 nm (see 2.2.2). As can be seen in the lower plot of figure 7.19, the radiation from the carbon atoms totally covers the Na I (3p-3s) emission and makes  $n_e$  evaluation by the Na beam diagnostic impossible for H discharges in ASDEX Upgrade.





## Chapter 8

# Conclusions

### 8.1 Results on expected advantages and disadvantages in Na beam operation

One of the main questions that had to be answered by this work was, if the Na beam shows the expected advantages during operation and why. So this part will discuss the expectations (listed in 2.2) and their realizations step by step based on the experimental results presented and discussed in chapter 7.

#### 8.1.1 Emitter temperature

It was expected, that the Na emitter temperature could be kept significantly lower than the Li emitter temperature. In fact, this expectation could not really be fulfilled. To achieve similar beam currents at same beam energies the Na emitter has to be heated up with approximately the same power as the Li emitter.

This fact also cancels the further expectations connected to a lower emitter temperature:

A higher current can not be achieved at temperatures equal to the Li beam, because these temperatures are already necessary to produce an equal current of up to 3 mA.

For higher voltages (60 kV) the Na emitter was expected to be more stable than the Li one. But for the Na emitter used in the third campaign this expectations could not be fulfilled, the emitter had to be kept at a rather low temperature to stay stable, leading to a lower beam current (1.7 mA) as compared to 50 kV. But due to experience on Li emitters of the same behavior this Na emitter of the third campaign is probably an outlier.

#### 8.1.2 Neutralization efficiency

The neutralization of the ion beam takes place in a sodium charge exchange cell. So advantages in neutralization efficiency were expected. For standard acceleration voltages of 40 or 50 keV both Na and Li beam are well neutralized. Rising the voltage to 60 keV would bring a significant advantage in Li beam penetration depth, but the neutralization efficiency gets much more down. For

	state	J	$\tau$ (s)	transition	J	$\lambda$ (nm)	$A_{ki}$ (s <sup>-1</sup> )
Na	$2p^6 3p$	$\frac{3}{2}$	$1.623 \cdot 10^{-8}$	$3p \rightarrow 3s$	$\frac{3}{2} \rightarrow \frac{1}{2}$	588.995	$6.16 \cdot 10^7$
Na	$2p^6 3p$	$\frac{1}{2}$	$1.629 \cdot 10^{-8}$	$3p \rightarrow 3s$	$\frac{1}{2} \rightarrow \frac{1}{2}$	589.592	$6.14 \cdot 10^7$
Li	$1s^2 2p$	$\frac{3}{2}$	$2.688 \cdot 10^{-8}$	$2p \rightarrow 2s$	$\frac{3}{2} \rightarrow \frac{1}{2}$	670.776	$3.72 \cdot 10^7$
Li	$1s^2 2p$	$\frac{1}{2}$	$2.688 \cdot 10^{-8}$	$2p \rightarrow 2s$	$\frac{1}{2} \rightarrow \frac{1}{2}$	670.791	$3.72 \cdot 10^7$

Table 8.1: Lifetime  $\tau$ , wavelength  $\lambda$  and Einstein coefficients  $A_{ki}$  for the IXS-observed Na and Li transitions

the Na beam the lower neutralization efficiency at  $60\text{keV}$  doesn't reduce the beam current that bad ( $1.7\text{mA}$  instead of  $2.5\text{mA}$ ), but on the other hand the penetration depth of Na is nearly constant in the region from 40 to  $80\text{keV}$ . So the overall evaluation depth and accuracy is not improved (see 7.3.2).

Summarized the advantages in neutralization efficiency at higher voltages are too low to cover the other disadvantages of higher voltages and therefore no general advantage arises.

### 8.1.3 Charge exchange cross sections

The charge exchange measurements were not part of this work. In general, however, it is clear that due to the different charge exchange cross sections of Na with impurities, advantages and disadvantages will occur depending on the impurity of interest.

### 8.1.4 Shorter transition lifetime

The lifetimes and wavelengths of the observed transitions of Na and Li IXS are given in table 8.1 (data out of [38]).

The lifetime of the observed Na I ( $3p\text{-}3s$ ) transition is 1.65 times shorter than of the Li I ( $2p\text{-}2s$ ) transition ( $26.9\text{ns}$ ). This causes a significantly lower occupation rate for the Na  $3p$  state as compared to the Li  $2p$  state (fig. 4.3) without lowering the emission intensity. The lower occupation of higher excited states in the Na beam reduces the beam attenuation, because the ionization rates are lower for the ground state than for the excited ones.

Strong benefits for density fluctuation measurements are therefore to be expected. This topic will be investigated in the future, see 8.2.5.

### 8.1.5 Effects of the different wavelength

#### Sensitivity of filter-PM setup

While the photomultipliers are more sensitive in the yellow region (Na I ( $3p\text{-}3s$ )) than in the red one (Li I ( $2p\text{-}2s$ )), the filter transmission  $T$  is slightly reduced for Na ( $T \approx 50\%$ ) as compared to Li ( $T \approx 60\%$ ). The reduced transmission for Na is due to the necessary suppression of the near He I line. Summed up the both effects cancel each other and neither the Na nor the Li beam gain any advantage within the filter-PM data acquisition.

### Radiation of thermal Na

Beside the fast Na atoms in the beam, also thermal Na, diffusing out of the neutralization cell, reaches the plasma edge. This Na also emits radiation, as can be seen in the spectra in fig. 2.6. It was expected that this background radiation may decrease the signal-to-noise ratio and increase  $n_e$  evaluation errors in the SOL region significantly, but this was never the case because the thermal Na background radiation is very small and is successfully subtracted together with the rest of the background.

#### 8.1.6 Atomic mass

The most important disadvantage concerning the penetration depth of the Na beam was expected to be the significantly higher atomic mass of 22.99 u (3.3 times the 6.94 u mass of Li). A non-relativistic calculation ( $v_{beam}^{Li} \approx \frac{1}{300}c$ ) gives a 1.82 times lower beam velocity in the case of Na than for Li at the same beam energy. This would mean that the penetration depth is reduced in the same order. Our experiments showed that the penetration depth is reduced by approximately 10 mm only (2% of  $\rho_{pol}$ ), depending on the discharge type (4.2).

#### 8.1.7 Lower ionization energy

The ionization energy for Na is slightly lower than that for Li. Regarding the influence of higher atomic mass and shorter transition lifetime the effects of the lower ionization energy are very low.

## 8.2 Summarizing the comparison to Li beam

### 8.2.1 Penetration and $n_e$ evaluation depth

The penetration depth of the Na beam is, as the LIN  $n_e$  evaluation depth, reduced by about 2 to 3% of  $\rho_{pol}$  as compared to the Li beam in H-Mode discharges. Nevertheless the Na beam penetration depth is sufficient to enable pedestal top  $n_e$  evaluation up to electron densities of  $8 \cdot 10^{19} \text{ m}^{-3}$ .

Using the conventional evaluation method (program absolut, diagnostic LID, using shooting method) instead of the new probabilistic evaluation algorithm (LIN), the difference in the position of the occurring singularity is lower than the difference in penetration depth, reducing the penetration depth disadvantage in this case. However, the new probabilistic algorithm delivers better results of higher accuracy for both Na and Li beam.

In L-Mode discharges the evaluation depth of the Na and the Li beam is almost equal.

### 8.2.2 $n_e$ evaluation quality

Concerning electron density evaluation of deuterium plasmas at ASDEX Upgrade, IDA is the state of the art diagnostic. It provides a full scale electron density profile, from the plasma core to the SOL, with high temporal and spatial resolution, especially in the ETB zone, where the data is provided by the Na / Li-IXS.

Comparing the quality of IDA  $n_e$  profiles, it is nearly equal for the Na and the Li beam. For both the error bars remain in the area of 5 to 15% up to pedestal top densities of about  $8 \cdot 10^{19} \text{ m}^{-3}$ . Here the only disadvantage of the Na beam is the increase of errorbars in the middle of the ETB zone during ELMs.

### 8.2.3 Non-standard plasmas

For He plasmas, the fear that the He I line at the edge of the transmitting filter wavelength interval would decrease the signal to noise ratio, is not justified. The filter specifications are good enough to keep the errorbars only about 1.5 times higher as compared to D plasmas. For the lithium beam there is a factor of 2. Additionally to the advantage in accuracy the Na beam is able to equal the penetration depth of the Li beam in He plasmas.

For H plasmas the Na beam can not be used for  $n_e$  evaluation, as long as methane  $\text{CH}_4$  is added to the plasma. The emitted CII line lying within the transmitting area of the filters makes it impossible to measure useful signals with the Na-IXS. H discharges without methane have not been carried out at ASDEX Upgrade during Na beam campaigns.

### 8.2.4 Influence on the plasma

The influence of the Na beam diagnostic on the plasma is very low. The interaction area is very tiny as compared to the plasma volume. The Na atoms brought into the plasma stay mainly in the ETB zone and do not enter the plasma center. Also the amount of Na, as well as the atomic number (11), is too low to play an important role as plasma impurity. No change in  $Z_{eff}$  is to be expected.

### 8.2.5 Future plans

It is expected that the shorter lifetime of the Na I (3p-3s) transition improves density fluctuation measurements which are conducted by a Hungarian research group at present [39].

Further the charge exchange capabilities (Na-CXS) should be explored.

There are also plans to change the present chopper setup to improve time resolution in order to be able to follow ELMs in time.

# Appendix A

## General appendix

### A.1 Sellmeier series equation

The sellmeier equation [40] describes the refraction index in dependence on wavelength  $\lambda$  by a fit

$$n^2(\lambda) = 1 + \sum_{i=1}^3 \frac{B_i \cdot \lambda^2}{\lambda^2 - C_i}$$

where the coefficients are determined by fitting the dispersion equation to measured values. The equation is valid (accuracy  $< 10^{-5}$  [26]) in the region of visible light and typically used for optical glasses.

#### A.1.1 beam coordinates

The table shows the absolute values of and the differences in the channel coordinates between the Li and the Na beam diagnostic due to the different refraction index. The values in the table are the theoretical coordinates, calculated with the theoretically exact optic geometry. It is clear, that the real coordinates differ slightly from these values. So the real coordinates were measured and calibrated for the Li beam 2p-2s emission wavelength. Out of these values the real coordinates for the Na beam emission 3p-3s were calculated using the piecewise linear transformation given by the theoretical coordinates in table A.1.

$$\begin{array}{ccc}
 x_{theor.}^{Li} & \leftrightarrow & x_{theor.}^{Na} \\
 & \Downarrow & \\
 & \text{piecewise} & \\
 & \text{linear} & \\
 & \text{transformation} & \\
 & \Downarrow & \\
 x_{real}^{Li} & \rightarrow & x_{real}^{Na}
 \end{array}$$

channel #	x Li [mm]	x Na [mm]	difference [mm]
1	0.6	-2.0	2.6
2	5.6	3.1	2.5
3	10.6	8.1	2.5
4	15.5	13.0	2.5
5	20.3	17.9	2.4
6	25.1	22.7	2.4
7	29.9	27.5	2.4
8	34.6	32.3	2.3
9	39.3	37.0	2.3
10	43.9	41.6	2.3
11	48.5	46.3	2.3
12	53.1	50.8	2.2
13	57.6	55.4	2.2
14	62.1	59.9	2.2
15	66.5	64.4	2.1
16	70.9	68.8	2.1
17	75.3	73.2	2.1
18	79.7	77.6	2.1
19	84.0	81.9	2.0
20	88.2	86.2	2.0
21	92.5	90.5	2.0
22	96.7	94.7	2.0
23	100.9	98.9	1.9
24	105.0	103.1	1.9
25	109.2	107.3	1.9
26	113.3	111.4	1.9
27	117.3	115.5	1.9
28	121.4	119.6	1.8
29	125.4	123.6	1.8
30	129.4	127.6	1.8
31	133.4	131.6	1.8
32	137.3	135.6	1.8
33	141.2	139.5	1.7
34	145.1	143.4	1.7
35	149.0	147.3	1.7

Table A.1: theoretical beam coordinates used for the piecewise linear transformation of the measured Li beam coordinates for the Na beam

## Appendix B

# Implementation of the main programs

### B.1 Implementation of the rate coefficient calculations

The calculation of the rate coefficients for collisions of Na with electrons and protons was implemented in two FORTRAN77-Subroutines, `elratna1-2.f` and `proratna1-2.f`. Because the two routines are very similar, `elratna1-2` will be described in detail and then only the differences in `proratna1-2` will be discussed.

The input ASCII-file `e-_param.ipp` contains the fit coefficients for all relevant cross sections [1]. The output ASCII-file `e-_raten` contains the spline coefficients for the cubic spline interpolating the excitation and ionization rate coefficients vs. electron temperature in 21 points between 1 and 10000 eV (compare fig. 6.1)

The program starts with an input part, where the user is asked for the beam energy. Then a loop covering all relevant processes starts, again with an input part, reading the fit coefficients from the input file. An inner loop runs through the 21 electron temperature points. Within this loop the integral (3.3) is evaluated as follows: The lower boundary for numerical integration is set to the velocity corresponding to the lower boundary  $E_{low}$  of the interval where the cross section fit is valid. If this lower boundary is greater than  $\Delta E_{i \rightarrow j}$ , a second lower boundary is introduced. If there is an effect on the value of the integral a warning is displayed. The upper boundary is set as the point where the exponential decreasing distribution function is at  $\frac{1}{1000}$  of its maximum value. After that the numerical integration is done by using the NAG-Library-Subroutine D01AJF. Finally the rate is divided by the beam velocity to get the reduced rate.

When these loops are done, there is an outer loop over states  $i$  and an inner one over states  $j$ . Within these loops the spline coefficients for the cubic spline interpolating the reduced rates are calculated using subroutines described in [41]. The output is also done within these loops. After them, the program ends.

The program `proratna1-2` uses `H+_param.ipp` as input file. There is also

an upper boundary for the upper boundary calculation, to avoid leaving the interval, where the cross section fit is valid. The fitting formulas for the proton cross sections differ a bit from the formulas for the electrons. For instance inner shell contributions to ionization have not to be taken into account. There is also a higher number of fit parameters. In the proton case the output file is called `H+_raten`.

To merge the data of the two output files and to format it, so that it can be directly used in the modeling and electron density calculation programs, the FORTRAN77-Subroutine `ratenblockna1-1.f` is used. It simply transfers the data from the 2 ASCII-Files into one FORTRAN BLOCK DATA Structure (file `raten[Eb].f`) that can be included in all FORTRAN programs that need the rate coefficients.

## B.2 Implementation of the beam attenuation modeling

The beam attenuation modeling is implemented in the FORTRAN77/shell script program `simula`, consisting of several modules. Some of these modules are also used for electron density evaluation in the FORTRAN77/shell script program `absolut` and the diagnostic `LID`. The newer diagnostics `LIN` and `IDA` use slightly modified modules and `Fortran95` is used.

The program `simula` consists of a shell script named `sim_na` and a compiled FORTRAN77 routine named `sim_[Eb]` (`[Eb]` is replaced by the beam energy in keV). In the following listing short descriptions are given and the differences to the old (Li-beam) modules are mentioned. All details are commented in the source code.

### shell script `sim_na`

The shell script `sim_na` handles the command line arguments and starts the program `simula`. It has to be called by "`sim_na Ebeam [Zeff-File] Outputfile zeff_abs [amatfile]`". If the arguments are not set, the user is asked for them or they are set to standard values. All relevant information is then written into the file `ein.dat` and finally the program with the defined beam energy is started.

### `Absolut.parameter`

Contains parameters. For the modeling only the first parameters, dimensions for arrays and the beam coordinate steps for the output-profile, are used. The other parameters control the shooting method in the program `absolut`, where the same parameter file is used (see B.3).

### `raten[Eb].f`

This is the BLOCK DATA file containing the reduced rate coefficient data. See also B.1.



**simimp\_na.f, simimp\_sub\_nav3-0.f**

The program `simimp` is the starting point, it calls the subroutine `simula` (in `simimp_sub_nav3-0.f`). Beside the main subroutine `simula`, some other functions and subroutines are contained in the file `simimp_sub_nav3-0.f`.

**lesen.f, te\_lesen.f, te\_spline.f**

The subroutine `dichte_lesen.f` reads the electron density input file `sim.dat`. The subroutine `Te_lesen` reads the electron temperature from the input file `W7.temp` while the function `Temp` returns the linear interpolated  $T_e$ -value.

**gitter\_nospline\_v1-0.f**

This file contains the 2 subroutines `A_Matrix` and `A_Matrix_dif` that calculate the A-Matrix  $a_{ij}$  and its differentiation by beam coordinate  $z$ .

The subroutine `A_Matrix` builds up the matrix by calling the routines in `modimp_nav1-0.f` and `zmod_nav1-0.f`, where the rate coefficients are derived. For the internal indexing the states Na 3s and Na 3p are exchanged, so that the occupation number of Na 3p stands in the first row of the solution vector of the differential equation. It has to be mentioned, that here the A-Matrix is calculated out of the reduced rates for each beam coordinate  $z$ . For a standard  $n_e$ -profile this calculation has to be done about 2000 times. In older versions used for the Li beam modeling only maximal 21  $z$  positions were evaluated and the intermediate values were provided by cubic spline interpolation. This was necessary due to the slower computers at that time. Nowadays it led to big errors in some cases where temperature profiles with a high gradient at the separatrix position and low SOL-temperature are used. Because of the badly chosen knots Matrices corresponding to negative temperature values occurred. To avoid these errors a direct evaluation was chosen for `simula`. For electron density evaluation, where a much higher number of evaluations is necessary, the interpolation was improved and even accelerated (see chapter 5).

In the old routines using cubic spline interpolation the differentiation of the A-Matrix by  $z$  was reduced to the differentiation of a polynomial in the interval between 2 knots. For the new A-Matrix-differentiation calculation the differential quotient is extrapolated by a rational extrapolation algorithm with 8 knots (distance of knot  $\#i$  to the evaluation position  $z$  is  $q^i, i = 1, \dots, 8$ ). This method reduces the error to a minimum, but costs 9 evaluations of the A-Matrix. It is not used in the modeling and only necessary in the shooting method (see 5.1, 5.2). So it was used to provide reference values for the accuracy test of the improved and accelerated interpolation method.

**modimp\_nav1-0.f**

An amount of functions is contained in this file. These functions provide the rates for all processes taken into account in the modeling and are called by the subroutines in `gitter_nospline_v1-0.f` that build up the A-Matrix. For the Zeff-modeling, the functions use functions in `zmod_nav1-0.f`.

### **zmod\_nav1-0.f**

Here the rates for collisions of Na beam atoms with impurity ions are calculated, using the formulas (3.7) - (3.12). Due to the scaling relations for some processes cross sections for energies below the valid energy range have to be used. These values for low energies are extrapolated out of values on the edge of the valid energy interval using simple formulas depending on the process.

## **B.3 Implementation of the program absolut**

The structure of the implementation is very similar to the implementation of the modeling in the program simula. The program absolut consists of a shell script named abs and a FORTRAN77 program with compiled name abs\_[Ebeam]. Some of the FORTRAN77 modules are also used in simula ( raten\_[Eb].f, te\_spline.f, modimp\_nav1-0.f, zmod\_nav1-0.f ) and were already described in B.2. Some other functions and subroutines are also the same or similar in both programs, but are in different modules / files. Again an overview is given, with focus on changes that were done. All details are commented within the source code.

### **shell script abs**

The shell script is the starting point of the program absolut. It has to be called with (optional) arguments by the command "abs Inputfile [Errorfile] [Ebeam] [Zeff-File] [global smooth factor] [central Zeff value]". The user may be asked for undefined arguments, otherwise standard values are used. The arguments and user data are then written into a file ein.dat to offer them to the FORTRAN77 program. Finally this FORTRAN77 program abs\_[Ebeam] is executed.

### **absmain\_nav1-0.f**

This file contains only the main program absolut. An enumeration of the major calculation steps and function/subroutine calls gives a good idea of the program structure:

**Definition and initialisation** At the begin the Absolut.parameter file is included, the main variables are defined and data values are initialized

**Reading data** At first the subroutine Dialog is called, where the data of fort.7 and ein.dat is read in. Then the data of the error file is extracted by the subroutine Lesen\_li\_rel. The subroutine lesen reads the emission profile in the given input file, and READFIT puts the data necessary for impurity ion rate calculation into common blocks. The next step is reading the  $Z_{eff}$ -profile by Zeff\_lesen and processing the data to splines for  $frac$  and  $q$  values.

**B-matrix** The B-matrix, consisting of the rates for spontaneous emission, is generated.

**Adding noise to the profile** This part of the program is not used in any more in the actual version, in the past it enabled to add some noise to profiles provided by modeling.

**Density calculation using different smooth factors** This option is also not used any more, only in older program versions.

**Some initialization and pre-calculation** At the beginning of the final big loop (in actual versions its contents is only executed once) some initialisation and calculations are done, preparing for the following steps.

**Smoothing the measured emission profile** In this part the measured line emission profile is smoothed. Therefore, one of two smoothing methods is chosen. The first option uses the NAG Fortran Library subroutine E02BAF, while the second one runs the FTSMOOTH subroutine (contained in `fourier.f`) first and then the NAG Fortran Library subroutine E02BEF. Both methods compute cubic spline approximations to the measured emission profile data set.

**Before starting the shooting method** Before the shooting method for determination of the factor  $\alpha$  is applied, the spline coefficients for the A-matrix are computed (by calling the subroutine `z_gitter_gen` in `gitter_linearv10.f`). Further it is tested if the nominator in (5.5) gets negative within the integration domain, because this indicates a singularity.

**Application of the shooting method** Within a while loop the shooting method is implemented, using the NAG Fortran Library subroutine D02CJF (containing a variable-order, variable-step Adams method) for solving the ODE. The functions and subroutine contained in `shootv3-1.f` are also used.

**Final density calculation** Finally the electron density is calculated using again the NAG Fortran Library subroutine D02CJF with the physical factor  $\alpha$  calculated in the prior step. The output is handled via the function output (call by reference by D02CJF).

### **diffglgv5-1.f**

Herein several subroutines and a function concerning the differential equation are contained. The subroutine `fcn` provides the right hand side of the differential equation (4.1). The subroutine `dens` calculates the density for a given Li2p emission profile. While the function `profil` offers the Li2p value at position  $z$ , the subroutine `diffpro` provides its first and second derivative at this position.

### **fourier.f**

The subroutine FTSMOOTH smoothes a linear real array by Fourier Transformation into frequency domain, cutting off the higher frequencies and finally applying the inverse Fourier Transformation. Parts of the algorithm are put into the other two subroutines that are contained in this FORTRAN-file.

### **gitter\_linearv1-0.f**

This file contains the subroutines that generate the A-matrix and its differential and provide them for the differential equation solvers and the shooting method routines. The subroutine `A_mat_gen` generates the A-matrix for a given  $z$ -coordinate and writes the data into a COMMON BLOCK array with given index

k. It uses the subroutines and functions in `modimp_nav1-0.f` and `zmod_nav1-0.f` and sums up the provided rate coefficients (see equations (4.3), (4.4)).

The subroutine `z_gitter_gen` generates a sequence of interpolation nodes for the A-matrix. If electron temperature changes more than  $100 \cdot T_e\_change \%$  (typically 20 %), a new node is set. To have enough nodes for flat  $T_e$ -profiles and to omit big errors in the SOL, a maximal distance between two neighbored nodes is defined (`maxstep`, typically 0.5 cm). After the node definition the A-matrix is generated by `A_mat_gen` at the nodes. Further linear interpolation coefficients corresponding to these data points are calculated and stored into a COMMON BLOCK array.

The subroutines `A_mat` and `A_mat_dif` calculate the interpolated A-matrix and its differential by  $z$  for a given beam coordinate  $z$ . They use the COMMON BLOCK data values produced by the subroutine `Z_gitter_gen`, the output is again written into a COMMON BLOCK. Beside the search for the interpolation interval index the numerical effort of both routines is very low (2 operations per matrix entry for `A_mat`, only an assignment per entry in `A_mat_dif`).

Up to this version of `absolut`, cubic spline interpolation with maximal 21 nodes and no maximal step was used for the A-matrix (file `gitterv4-0.f`). This caused problems for certain temperature profiles with steep gradients, where A-matrices corresponding to negative temperatures in the SOL were produced. In the actual version this problems can not occur. The numerical effort also decreased (old version: 6 operations per matrix entry for both subroutines). The accuracy could be kept equivalent or even raised by increasing the number of nodes to a maximum of 50. Here some tests were made by comparing the solutions to reference profiles produced by using `gitter_nospline_v1-0.f`. Another advantage is the better correspondence to the interpolation of the temperature profile, that has been changed from cubic to linear splines already before.

### **inout\_nav1-0.f**

Contains Subroutines for input and output.

### **method2v5-2\_augd.f**

The contained subroutines `dichte` and `diff`, as well as the function `lambda`, are used for electron density calculations using the so-called "2nd method".

### **read\_nav1-0.f**

Contains the subroutine `lesen`, that reads the emission profile out of the given input file, and the subroutine `zeff_lesen`, that reads the  $Z_{eff}$ -profile. `zeff_lesen` has been changed so that its the same as the subroutine `zeff_lesen` in the program `simula`. This reduces the risk of systematic errors in  $Z_{eff}$ -calculations and simplifies program improvements.

### **read\_errorv2-0.f**

Contains the subroutine `lesen_li_rel`, that reads the relative error of the emission profile out of the error-file.

#### **reff.f**

Contains the function reff that returns 0.

#### **shootv3-1.f**

Contains the functions next\_fak and kappa as well as the subroutine analyze. These are part of the shooting method implementation.

## **B.4 Changes in the implementation of the new probabilistic evaluation algorithm**

As for the conventional Li beam electron density algorithm changes had also to be done in the new probabilistic evaluation algorithm, used for diagnostic LIN, IDA [35].

Here all modules and changes within them are listed:

**Mod\_lib\_atomic** N\_Li0 (number of Li/Na states) change from 9 to 8.  
changing the number of states also in read\_rate and its debug part.

**Mod\_lib\_zmod** Taken over from zmod\_nav1-0.f, changed to FORTRAN90/95, warnings are commented out.

**Mod\_lib\_modimpv** Changing all  $Z_{eff}$  parts like in modimp\_nav1-0.f: zex + zex3l  $\rightarrow$  ZEXsigma, zion + zxcxs  $\rightarrow$  ZELOSS.

Changing the Einstein coefficients from Li to Na.

The variable tempdim\_max has been used for both A\_Matrix (initial intention) as well as for rate coefficient interpolation node numbers. For the rate coefficients the number of nodes is now fixed at 21, because this number is also fixed by the rate input files and the interface between these two programs is not intended to be changed. This leads to the possibility of individual change of the A\_Matrix interpolation node number as well as the interpolation order. Tests in program absolut have already shown advantages in numerical effort and accuracy using linear interpolation with about 50 nodes.

**Mod\_libe** After calling read\_rate in read\_lid\_params the subroutine READ-FIT is now additionally called. This subroutine reads the values necessary for  $Z_{eff}$  parts.

**Libe\_utils** Possible changes to linear interpolation with 50 nodes, maximal node distance 5 mm and maximal change in  $T_e$  20%.

**Libe.inp** Important input file. Change of the parameter directory and the ion mass. Out of the parameter directory important data like spatial position of the observed signals and rate files are used.

**additional changes**

There are also a few very tiny changes not mentioned here, like in initialization or change of variable types. Concerning the overall evaluation program after the implementation of the Na version like described here it is merged with the Li version using a selection parameter `type_ion` that is set to 'Na' or 'Li', depending on the shot number. Therefore the shotnumbers where the emitter is changed from Na to Li or the other way around are logged.

## Appendix C

# Programs used for data processing, evaluation and visualization

Additionally to the programs described up to now, several IDL and MATLAB programs were written and used for data processing, evaluation and visualization. While the FORTRAN programs are used mainly for the numerical algorithms and basic calculations, the IDL programs operated one step above, providing data for the FORTRAN programs and postprocessing the results. The MATLAB functions written for this work were then mainly used in the final step of evaluation and visualisation.

All programs and functions used in this work are contained in the DVD and non-trivial code is well commented, so that a detailed description of all programs is not necessary here.

### C.1 IDL programs

IDL programs were mainly written for two purposes:

1. for calling the FORTRAN programs `simula` and `absolut` with the right options and parameters, including pre- and postprocessing tasks.
2. for access to the ASDEX Upgrade database, meaning evaluation of the data provided by the several diagnostics mentioned in this work (as LIA, LIB, ..., IDA).

### C.2 MATLAB functions

A broad amount of MATLAB functions was produced for data file reading, data processing and data visualization. All used functions are contained in the MATLAB directory at the DVD. Here the types of used functions are described.

### C.2.1 data reading functions

These functions read data out of ASCII files that are provided by FORTRAN or IDL programs and containing electron density profiles, for example. The data is then put into variables (mainly matrices) for further processing and visualization.

### C.2.2 data processing functions

These functions are sorting, averaging, transforming or grouping data sets. An example is the piecewise linear transformation of data values or the calculation of penetration/evaluation depths as defined in 7.2.1.

#### piecewise linear transformations

Very simple, but useful functions imaging  $x$  (a single value of an array of values) to  $y$  via a piecewise linear function that is given by a table of discrete  $x$  and  $y$  values. In this work these functions are often used for transformations between different one dimensional coordinates, like beam coordinate  $x$ , major radius  $r_{maj}$ , midplane radius  $r_{midplane}$  and normalized poloidal radius  $\rho_{pol}$ .

### C.2.3 plotting functions

After the data is prepared the plotting functions visualize it. Title and legends are automatically generated depending on discharge type and number, for instance. Most figures in this work were generated using these MATLAB functions.



# Bibliography

- [1] K. Igenbergs et Al. Database for inelastic collisions of sodium atoms with electrons, protons, and multiply charged ions. *Atomic Data & Nuclear Data Tables*, 94:981–1014, 2008. doi: 10.1016/j.adt.2008.06.001.
- [2] Jeffrey P. Freidberg. *Plasma Physics and Fusion Energy*. Cambridge University Press, The Edinburgh Building, Cambridge CB2 8RU, UK, 2007.
- [3] Wolfrum E. Schweinzer J. Vorlesungsunterlagen zur Vorlesung 134.750 'Phys. Grundlagen d. Kernfusionsreaktors' an der TU wien im SS 2007, 2007.
- [4] The ASDEX Upgrade Team. ASDEX Upgrade Intranet: Documentation: Machine: Pictures, description and details:AUG.
- [5] E. Wolfrum, F. Aumayr, J. Schweinzer, and R. Fischer. E-Mail Correspondance.
- [6] B. Kurzan, H. Murmann, and H. Salzmann. Improvements in the evaluation of Thomson Scattering data on ASDEX Upgrade. *Review of Scientific Instruments*, 72:1111–1114, 2001.
- [7] B. Kurzan. Signal processing of Thomson Scattering data in a noisy environment in ASDEX Upgrade. *Plasma Physics and Controlled Fusion*, 46(1):299–317, 2004.
- [8] A. Silva, M. E. Manso, L. Cupido, M. Albrecht, F. Serra, P. Varela, J. Santos, S. Vergamota, F. Eusébio, J. Fernandes, T. Grossmann, A. Kallenbach, B. Kurzan, C. Loureiro, L. Meneses, I. Nunes, F. Silva, and W. Suttrop ASDEX Upgrade Team. Ultrafast broadband frequency modulation of a continuous wave reflectometry system to measure density profiles on ASDEX Upgrade. *Review of Scientific Instruments*, 67(12):4138–4145, 1996.
- [9] G.D. Conway. Doppler reflectometry on ASDEX Upgrade: Foundations and latest results. *Proceedings of the 8th International Reflectometry Workshop (IRW 8)*, pages 30–36, 2007.
- [10] E. Galutschek et Al. Development of fast Helium beam emission spectroscopy for Tokamak plasma density- and temperature diagnostics. *EFDA-JET-CP*, pages 1–18, 2003.
- [11] H.D. Falter et Al. Helium doped hydrogen or deuterium beam as cost effective and simple tool for plasma spectroscopy. *Review of Scientific Instruments*, 71(10):3723–3727, October 2000.

- [12] H.D. Falter et Al. Helium doped Hydrogen or Deuterium beam as cost effective and simple tool for plasma spectroscopy. *Fusion Engineering and Design*, 56-57:941–946, 2001.
- [13] R. Brandenburg et Al. Modelling of fast neutral Li beams for fusion edge plasma diagnostics. *Plasma Phys. Control. Fusion*, 41:471–484, 1999.
- [14] S. Fiedler, R. Brandenburg, J. Baldzuhn, K. McCormick, F. Aumayr, J. Schweinzer, HP. Winter, and W7AS & ASDEX Upgrade Team. Edge Plasma Diagnostics on W7-AS and ASDEX Upgrade using fast Li Beams. *Journal of Nuclear Materials*, 266-269:1279–1284, 1999.
- [15] R. Brandenburg et Al. Li(2p  $\leftarrow$  2s) excitation by impact of slow ions. *J. Phys. B: At. Mol. Opt. Phys.*, 31:2585–2599, 1998.
- [16] E. Wolfrum et Al. Fast Lithium-beam spectroscopy of tokamak edge plasmas. *Review of Scientific Instruments*, 64:2285–2292, 1993.
- [17] I. Nunes. Density measurements with combined Li-Beam diagnostics and microwave reflectometry during advanced tokamak operation on ASDEX Upgrade. *Europhysics Conference Abstracts (CD-ROM), Proc. of the 26th EPS Conference on Controlled Fusion and Plasma Physics*, 23J:1633–1636, 1999.
- [18] E. Wolfrum et Al. A sodium (Na) beam edge diagnostic. *Journal of Nuclear Materials*, In Press, Corrected Proof, 2009.
- [19] E. Wolfrum, J. Schweinzer, M. Reich, L. D. Horton, and C. F. Maggi. Impurity ion density measurements at the plasma edge of ASDEX Upgrade using lithium beam charge exchange spectroscopy. *Review of Scientific Instruments*, 77(3):033507, 2006.
- [20] R. P. Schorn et Al. Absolute concentrations of light impurity ions in tokamak discharges measured with Lithium-beam-activated charge-exchange spectroscopy. *Applied Physics B*, 52:71–78, 1991.
- [21] E. Unterreiter et Al. Multicharged ion-atom collisions - application for tokamak edge plasma physics. *J. Phys. D: Atoms, Molecules and Clusters*, 21:167–168, 1991.
- [22] M. Reich. Lithium beam charge exchange diagnostic for edge ion temperature measurements at the ASDEX Upgrade Tokamak. *Plasma Physics and Controlled Fusion*, 46(5):797–808, 2004.
- [23] F. Aumayr and Hannspeter Winter. Plasmadiagnostik mit Lithiumatomstrahl-aktivierter Umladungsspektroskopie. *Annalen der Physik. 7. Folge*, 42(3):228–238, 1985.
- [24] E. Wolfrum, B. Langer, R. Fischer, and ASDEX Upgrade Team. Determination of the radial electric field from passive He II emission. *Europhysics Conference Abstracts*, 32D:O2.002, 2008.

- [25] Josef Kamleitner. Weiterentwicklung von IDL-Auswerteroutinen für Natriumstrahl-Diagnostik und Anwendung auf aktuelle Messungen, September 2007. Protokoll im Rahmen einer Werkstudententätigkeit am IPP in Garching.
- [26] Schott. Optical glass datasheets, 10 2007. <http://tinyurl.com/schott200710ogd>.
- [27] M. Schneider. Beiträge zur Untersuchung von Tokamak-Randschichtplasmen mittels aktiver Li-Atomstrahlen. Master's thesis, Technische Universität Wien, 1990.
- [28] J. Schweinzer et Al. Two programs for calculations of collisional atomic data for Lithium beam plasma spectroscopy. *Computer Physics Communications*, 88:83–88, 1995.
- [29] D. Wutte, R.K. Janev, F. Aumayr, M. Schneider, J. Schweinzer, J.J. Smith, and HP. Winter. Cross Sections for Collision Processes of Li Atoms Interacting With Electrons, Protons, Multiply Charged Ions, And Hydrogen Molecules. *Atomic Data & Nuclear Data Tables*, pages 155–180, 1997.
- [30] J. Schweinzer et Al. Database for inelastic collisions of Lithium atoms with electrons, protons, and multiply charged ions. *Atomic Data & Nuclear Data Tables*, 72:239–273, 1999.
- [31] H. J. Hartfuss, T. Geist, and M. Hirsch. Heterodyne methods in millimetre wave plasma diagnostics with applications to ECE, interferometry and reflectometry. *Plasma Phys. Control. Fusion*, 39:1693–1769, 1997.
- [32] N.A. Salmon. First electron temperature edge measurements on the ASDEX Upgrade tokamak using a heterodyne radiometer. *International Journal of Infrared and Millimeter Waves*, 15(1):53–60, 1994.
- [33] N.K. Hicks. Measurement of NTMs, modulated ECRH deposition, and current ramp-up MHD activity using the upgraded 1 MHz ECE radiometer on ASDEX Upgrade. *Europhysics Conference Abstracts*, 32D:P–4.082, 2008.
- [34] J. Schweinzer, E. Wolfrum, F. Aumayr, M. Pöckl, H. Winter, R.P. Schorn, E. Hintz, and A. Unterreiter. Reconstruction of plasma edge density profiles from LiI(2s-2p) emission profiles. *Plasma Physics and Controlled Fusion*, 34:1173–1183, 1992.
- [35] Rainer Fischer. Probabilistic lithium beam data analysis. *Plasma Phys. Control. Fusion*, 50(8):26, August 2008.
- [36] R. Fischer. Integrated density profile analysis in ASDEX Upgrade H-modes. *Europhysics Conference Abstracts*, 32D:P–4.010, 2008.
- [37] Wolfrum E. Schweinzer J. Logbuch der Lithiumstrahldiagnostik am ASDEX Upgrade.
- [38] Yu. et Al. Ralchenko. NIST atomic spectra database (version 3.1.3), [online]. available: <Http://physics.nist.gov/asd3> [2007, september 20]. Technical report, National Institute of Standards and Technology, Gaithersburg, MD, 2007.

- [39] Pusztai István et Al. Capabilities of alkali beam emission spectroscopy for density profile and fluctuation measurements. *34th EPS Conference on Plasma Phys. Warsaw, 2 - 6 July 2007 ECA Vol.*, 31F:P2.137, 2007.
- [40] W. Sellmeier. Zur Erklärung der abnormen Farbenfolge im Spectrum einiger Substanzen. *Annalen der Physik und Chemie*, 143:271, 1871.
- [41] Helmuth Spaeth. *Spline-Algorithmen Zur Konstruktion Glatter Kurven und Flaechen*. Oldenburg, 1973.

## Danksagung

Mein primärer Dank gilt Prof. Dr. Friedrich Aumayr, der mir diese Diplomarbeit samt Aufenthalt in Garching ermöglichte und sie sehr gewissenhaft betreute. Mein besonderer Dank gilt Dr. Elisabeth Wolfrum, welche mich in Garching am IPP immer unterstützte und auch danach bei Fragen zur Verfügung stand. Weiters möchte ich Dr. Josef Schweinzer danken, nicht nur für die gute Zusammenarbeit in Garching, auch dafür, dass er mich gemeinsam mit Dr. Elisabeth Wolfrum durch die Vorlesung "physikalische Grundlagen des Kernfusionsreaktors" für dieses Thema faszinieren konnte.

Auch die weiteren Mitarbeiter des IPP in Garching waren immer sehr hilfbereit und kollegial, erwähnen möchte ich hier auch Dr. Rainer Fischer und seine Kompetenz im Bereich der neuen Auswerteroutinen der Lithiumstrahl Diagnostik.

Mit den Mitgliedern der Arbeitsgruppe von Prof. Dr. Friedrich Aumayr verbinden mich ebenfalls nur positive Erfahrungen. Hier möchte ich mich im Besonderen bei Dipl.-Ing. Katharina Igenbergs bedanken, welche nicht nur durch ihre Diplomarbeit den Weg für die meinige ebnete, sondern mir auch jederzeit mit Rat und Tat zur Seite stand.

Neben diesen direkt beteiligten Personen möchte ich mich auch noch bei allen anderen für die moralische und sonstige Unterstützung danken, vor allem aber bei meiner Familie und meinen Freunden.